Geophysical Journal International

Geophys. J. Int. (2018) **216,** 1798–1816
Advance Access publication 2018 November 30
GJI Seismology

doi: 10.1093/gji/ggy510

Reviving m_B

Hiroo Kanamori and Zachary E. Ross

Seismological Laboratory, California Institute of Technology, Pasadena, CA 91125*, USA. E-mail: hiroo@gps.caltech.edu*

Accepted 2018 November 28. Received 2018 November 8; in original form 2018 June 13

SUMMARY

We determine m_B, the original body wave magnitude developed by Gutenberg and Richter over the period 1942–1956, for about 3300 $M_w \geq 6$ earthquakes for the period 1988–present using modern broad-band seismograms. The main objective is to extend the database of energy-related parameters by combining m_B databases for recent and old events. The radiated energy E_{R_B} (in erg) computed from m_B using the Gutenberg & Richter relation $\log E_{R\_B} = 2.4m_B + 5.8$ agrees very well with E_R estimated with modern techniques, especially for large deep earthquakes. Thus, E_{R_B} is useful as a proxy for E_R to investigate the global diversity of earthquake characteristics and physics over an extended period of time.

Key words: Body waves; Earthquake dynamics; Earthquake hazards; Earthquake source observations; Wave propagation; Subduction zone processes.

INTRODUCTION

Gutenberg (1945a, 1945b) and Gutenberg & Richter (1942, 1956a,b) developed a body wave magnitude m_B using the body wave amplitude recorded on classic seismographs such as Wiechert, Galitzin, Mainka, Milne Shaw, and Benioff seismographs. Their objective was to estimate the radiated energy from observed seismic body waves for earthquake quantification purposes and for better understanding of earthquake physics. Details on the historical development of the concept, method, difficulties, and caveats are described in Richter (1958, pages 338–374). Also, a detailed survey of history on this subject can be found in Okal (2018). Unfortunately, routine determination of m_B was discontinued in the 1960s and earthquake energy parameters became less commonly available (e.g. Storchak *et al.* 2015; Di Giacomo & Storchak 2016).

Since the inception of global seismic networks like the analogue World-Wide Standardized Seismographic Network (WWSSN) and digital broad-band seismograph networks, efforts to accurately estimate radiated energy were revived using modern seismological practices (e.g. Boatwright & Choy 1986; Kikuchi & Fukao 1988). In the modern practice of energy estimation, many factors such as radiation pattern, spatial variation of attenuation, broad-band source spectra, and complex propagation effects are considered. These factors were not addressed in the studies of Gutenberg and Richter and many other early investigators because of instrumental and computational limitations. Yet, there are still significant unresolved issues such as the complex interference effect between direct and surface-reflected phases, as well as the scattering of energy. Another difficulty in using teleseismic waves is that the *S* waves that carry most of the radiated energy are severely attenuated during propagation, and except in a few cases (e.g. Baltay *et al.* 2014), cannot be used for energy estimation. Thus, commonly only *P* wave energy is measured and at the end it is multiplied by a large factor (typically 15–25) to estimate the total energy. This practice is not entirely satisfactory. Nevertheless, significant efforts have been made to improve the method so that the accuracy of teleseismic energy estimates is now good enough to investigate the global diversity of earthquakes. This will improve our understanding of earthquake physics and allow for more effective hazard mitigation practices (e.g. Kanamori 2014).

However, the presently available E_R database includes only recent events, and it is desirable to link the results from recent studies to those from old studies. Since m_B is available for many important old events before 1990, it would be useful to determine m_B for recent events to understand global seismicity on a longer time scale. Such an effort was recently made for the 2017 Chiapas, Mexico earthquake, the 1931 Oaxaca earthquake and the 1933 Sanriku earthquake (Ye *et al.* 2017). Comparison of these events helped to understand the global significance of large lithospheric earthquakes.

Bormann & Saul (2008) emphasized the value of the IASPEI body wave magnitude, m_B(BB), for which a recommended standard procedure had been adopted by the IASPEI Commission on Seismological Observation and Interpretation in 2005 (IASPEI 2005). The IASPEI m_B(BB) procedure departs somewhat from Gutenberg and Richter's m_B procedure, notably in the IASPEI procedure's use of amplitude measurements made from a velocity-proportional signal: in our work we try to closely follow Gutenberg and Richter's procedure so that we can directly compare old and recent events. m_B and m_B(BB) should be regarded as different scales with different objectives.

The purpose of this study is twofold:

(1) Build a catalogue of m_B for events with $M_w \geq 6$ for the period 1988–present using modern broad-band records. This catalogue can be used for general research on global seismicity over a longer period of time.

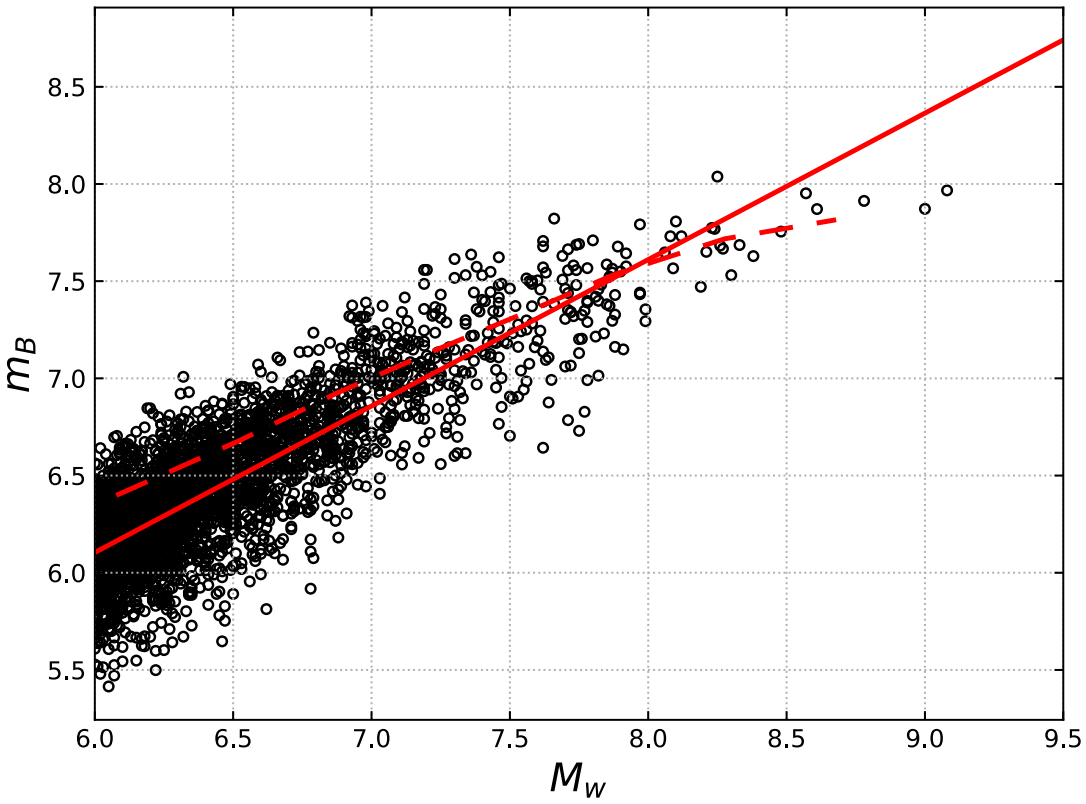

Figure 1. Relation between m_B and M_w. The solid red line indicates the general trend, $m_B = 0.75M_w + 1.63$, and the dashed red line is the relation between m_B and M_w for old events (Kanamori 1983).

(2) Present a few notable features on the diversity of global seismicity that can be revealed from energy-related parameters derived from m_B.

METHOD

We try to closely follow the procedure of Gutenberg and Richter (for details see e.g. Geller & Kanamori 1977; Abe 1981; IASPEI 2013). They used primarily the body wave peak amplitude, A_p, and period, T_p, reported in station bulletins from many observatories around the world. Then, m_B is given by

$$m_B = \log_{10}(A_p/T_p) + Q(\Delta, h), \quad (1)$$

where $Q(\Delta, h)$ is a function of distance Δ and depth h determined empirically by Gutenberg and Richter from large amounts of amplitude measurements. This function is shown graphically in Richter (1958) and has been tabulated by IASPEI (2013). Gutenberg & Richter used various body wave phases such as *P*, *PP*, and *S* recorded on both vertical and horizontal component seismograms with a period of typically from 1 to 10 s.

In implementing this method in this study, we take advantage of modern digital records and modify the method slightly. We use only *P* waves recorded on the vertical component. We first compute the ground motion displacement by removing the instrument response. Then we convolve it with the response of a Wiechert-type seismograph with a pendulum period $T_s = 3.5$ s, a damping ratio $\varepsilon = 4.5$ and a static gain of 1 to simulate the seismograms used by Gutenberg & Richter. The Wiechert response is chosen as a representative response. We use the vertical component because it is the well-defined component of *P* waves. Also, the attenuation function, Q, for the vertical component has been most widely used and is available in digital form. The choice of $T_s = 3.5$ s is appropriate for vertical component records. Another reason for our choice of $T_s = 3.5$ s is that we want to include events down to $M_w = 6$. The source duration is about 6 s for $M_w = 6$, and we want to have at least a few cycles of oscillation in the windowed wave train. If we choose $T_s = 10$ s, we would have too few cycles in the *P*-wave window. For large earthquakes, we could have used a larger T_s, but to mix up different T_s for small and large earthquakes would introduce undesirable complexity in the database.

In practice, Gutenberg & Richter used many seismic phases recorded with many different types of seismographs. Since most vertical component seismographs were relatively short period, typically 1 to 3 s, the vertical component of *P* wave amplitude was measured at 1 to 3 s, while the amplitude measurements of other phases were often made on long period horizontal seismograms, which were typically 4 to 20 s. Thus, m_B is actually a parameter with very heterogeneous properties, but it appears that Gutenberg & Richter, with a strong desire to have just one parameter, m_B, calibrated the measurements from different types of phases and instruments by adjusting the Q functions. In this work, we simplify the procedure by using only vertical component *P* waves recorded on a Wiechert-type seismograph. If desired, we can easily use any other types of instruments, but as we will show later, as long as the response is reasonably broadband (similar to that of old mechanical instruments), the result remains essentially the same.

For the period measurement, we determine the instantaneous frequency of the simulated Wiechert record continuously in time using the method described in Nakamura (1988) and Kanamori (2005) as detailed in Appendix A, as opposed to the period measurements manually done on analogue recordings by station seismologists (see

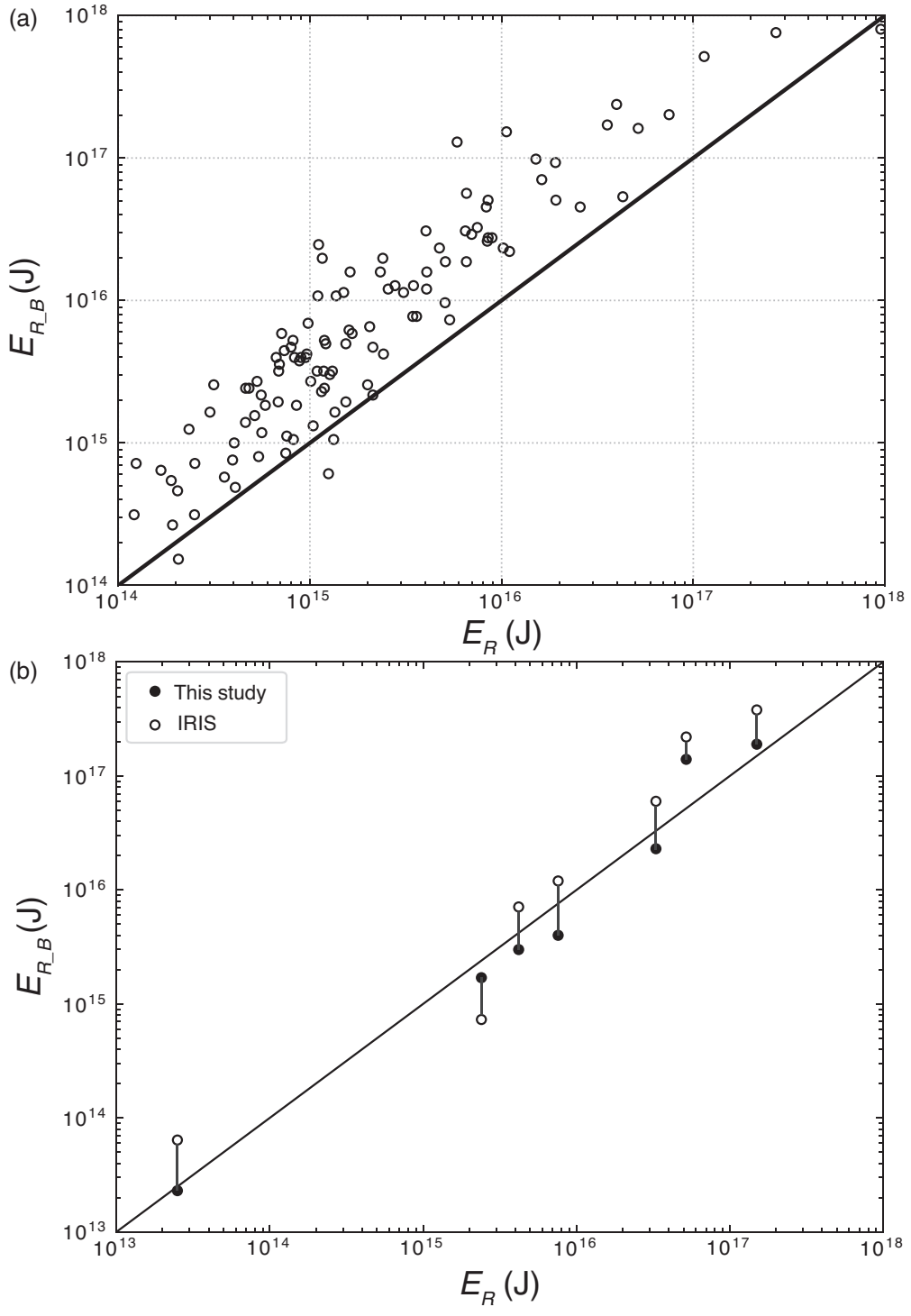

Figure 2. (a) Comparison between the radiated energy E_R estimated by Ye *et al.* (2016b) and that estimated from m_B, E_{R_B}, for large megathrust earthquakes. (b) Comparison between the radiated energy E_R and E_{R_B} for seven deep earthquakes. E_R values listed in Table 1 are on the abscissa, and E_{R_B} (closed circle) from this study are on the ordinate. For comparison, E_R values from IRIS EQEnergy database are also shown on the ordinate (open circle). The solid line indicates the relation $E_{R\_B} = E_R$.

e.g. figure 3.19 of Bormann *et al.* 2013). We measure the amplitude and period of the largest phase on the Wiechert seismogram, and divide the amplitude by the instrument gain at the period of the peak phase to determine the ground motion amplitude A_p. The duration of the signal, T_d, to be used is determined by the smaller of $3t_c$ and PP−P time (*PP* minus *P* traveltime) where t_c (in s) is the centroid time of the source time function estimated by $t_c = 1.2 \times 10^{-8} M_0^{1/3}$ (M_0 is the seismic moment in dyne cm) (Duputel *et al.* 2013). When t_c is measured directly from waveform inversion, it can also be used. With this modification, we can measure m_B objectively and robustly.

Table 1. Radiated energy of deep earthquakes.

Event	Depth, km	M_w	E_R	E_R (From IRIS EQEnergy)	E_{R_B}	Reference for E_R
1994 Bolivia	637	8.2	5.4e16	2.2e17	1.4e17	Winslow & Ruff (1999), This study[a]
2010 Spain	610	6.4	2.5e13	6.4e13	2.3e13	This study
2013 Okhotsk	598	8.3	1.5e17	3.8e17	1.9e17	Ye *et al.* (2013)
2013 Okhotsk	624	6.7	2.4e15	7.3e14	1.7e15	Ye *et al.* (2013)
2015 Bonin	664	7.9	3.3e16	6.0e16	2.3e16	Ye *et al.* (2016d)
2015 Peru-Brazil	601	7.6	4.2e15	7.1e15	3.0e15	Ye *et al.* (2016c)
2015 Peru-Brazil	612	7.7	7.6e15	1.2e16	4.0e15	Ye *et al.* (2016c)

[a]Winslow & Ruff's (1999) estimate is from a time domain method, and a correction is applied for the attenuation effect.

Gutenberg & Richter (1955, 1956a) estimated the radiated energy E_{R_B} using the relation,

$$\log_{10} E_{R\_B} = 5.8 + 2.4 m_B \quad (E_{R\_B} \text{ in erg}). \tag{2}$$

Because of the inevitable limitations in instrumentation and computing facility, estimates of the radiated energy from m_B are only approximate. It does not account for the radiation pattern, explicit source spectrum and bandwidth or complex propagation effects. Nevertheless, Gutenberg & Richter made every possible effort to calibrate it against the energy measured locally. In the local estimate, *S* waves that carry nearly 95 per cent of the total energy were used. They also implicitly included some scaling effects (relation between amplitude and duration) in deriving eq. (2). Thus, despite the simplicity of the method, the energy estimate from m_B can serve as a useful proxy for the radiated energy as we will show in the next section. The symbol E_{R_B} means that it is a proxy for the real radiated energy E_R. This convention will be used throughout this paper.

DATA

We first selected all earthquakes with $M_w \geq 6$ (1988–present; last accessed 2018 March) from the global CMT catalogue (www.globalcmt.org, Dziewonski *et al.* 1981; Ekström *et al.* 2012), which totals 3587 earthquakes. The M_w used in this paper is all taken from the GCMT catalogue.

For these events, we downloaded data from IRIS (Incorporated Research Institutions for Seismology) for all Federation of Digital Seismograph Network and Global Seismographic Network stations on BHZ channels at distances in the range 30°–80°. The seismograms were windowed starting 5 s before the predicted *P*-wave arrival and ending T_d s after. We use mostly PDE locations to compute the predicted *P*-wave arrivals.

RESULTS AND CALIBRATION

We determine m_B for 3317 $M_w \geq 6$ events and the resulting catalogue is given in Table S1 (Supporting Information). The catalogue lists, for each event, year, month, day, hour, min, second, Event ID, latitude, longitude, hypocentre depth, M_w, average m_B, the standard deviation m_{B_std}, median m_{B_md}, average period, T_p, standard deviation T_{p_std}, median period, T_{p_md}, the number of stations used, n, the mechanism parameter, C_m (Shearer *et al.* 2006), M_0, E_{R_B}, scaled energy, centroid depth and apparent stress.

The catalogue is intended for general research on global variation of earthquake source characteristics. As a form of quality control, we exclude events for which $m_{B\_std} > 1$, $T_p > 6$ s and $n \leq 10$. Some details of our screening process are given in Supporting Information S1.

Fig. 1 shows m_{B_md} as a function of M_w for all the events. Hereafter we use m_{B_md} as m_B. The red dashed curve is the relationship between M_w and m_B for old events (Kanamori 1983; Utsu 2002). Although there is a small difference, the overall trend is the same between the old and new data sets which assures that despite the difference in the method, the two data sets have essentially the same basis and can be compared directly. The solid red line (slope = 0.75) indicates the overall trend given by

$$m_B = 0.75 M_w + 1.63. \tag{3}$$

The slope gradually decreases to 0.5 with increasing M_w. Abe (1982) obtained a similar trend for past deep earthquakes. For events with $M_w \leq 7.8$, the scatter of m_B for a given M_w is approximately the same. Since the computation of m_B is straightforward and robust, this scatter probably reflects the real diversity of earthquake characteristics. For events with $M_w \geq 7.8$, the number of events is too small to establish the range of scatter.

Comparison of E_{R_B} with the radiated energy E_R estimated for recent events

Given all the inevitable limitations of E_{R_B}, the first question is how E_{R_B} compares with E_R measured with modern techniques for recent events using broad-band records. In Fig. 2(a), we compare E_{R_B} thus estimated with E_R for recent large events determined by Ye *et al.* (2016b). Except for only a few events, the ratio E_{R_B}/E_R is almost constant at about 3. The factor of 3 difference is not surprising given the many simple assumptions made in energy estimation. Ye *et al.* (2018) compared their data set with the E_R data sets available from IRIS EQEnergy (IRIS DMC 2013, https://ds.iris.edu/spud/eqenergy) and USGS NEIC (fig. S5 of Ye *et al.* 2018). On average, the energy estimates from IRIS and the NEIC data base are about 80 per cent and 40 per cent, respectively, of that of Ye *et al.* (2016b) data base. This suggests that we still have some discrepancy in the absolute value of energy between different data sets, but the similarity of the trend suggests that the difference is mainly in the scale factor associated with the details of the model parameters. Fig. S1 of the Supporting Information shows a direct comparison between E_{R_B} and E_R given in the IRIS data base (https://ds.iris.edu/spud/eqenergy). Thus, despite the limitation of m_B, E_{R_B} can be a useful proxy for the energy when the relative value is the subject of interest.

Fig. 2(b) compares E_{R_B} with E_R for seven deep earthquakes for which we have independent determinations (Table 1). The agreement is very good, which is surprising considering that E_R of large earthquakes like the 1994 Bolivia and 2013 Okhotsk earthquakes

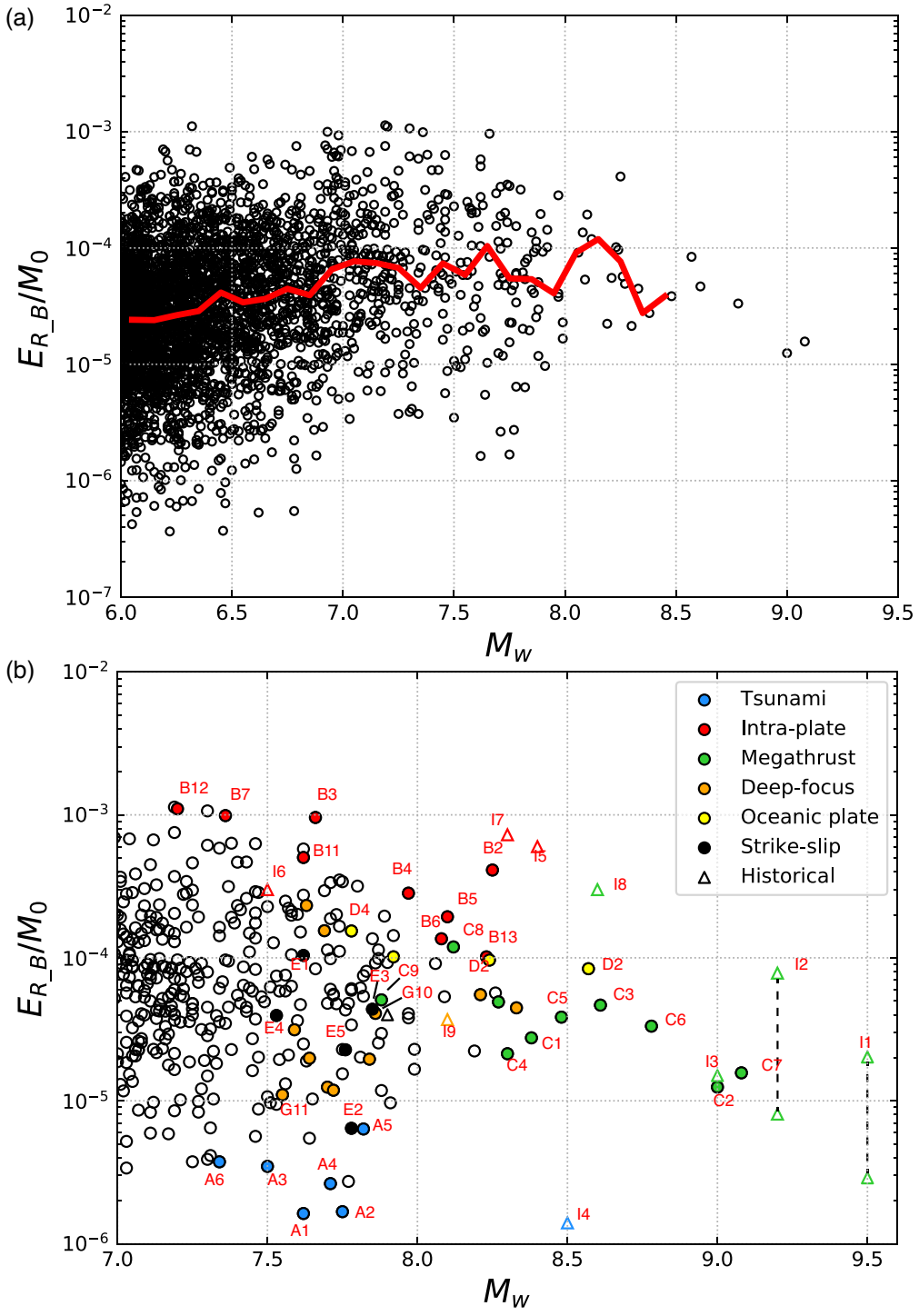

Figure 3. (a) Scaled energy (E_{R_B}/M_0) versus M_w. The red curve shows the median value. (b) Same as (a) for $M_w \geq 7$ earthquakes. Some notable earthquakes are marked by different colours. Blue: Tsunami earthquakes; Red: Intraplate earthquakes (outer-rise normal-fault and thrust earthquakes, large earthquakes within subducting oceanic plates); Green: Megathrust earthquakes; Orange: Deep earthquakes; Yellow: Large strike-slip earthquakes in the oceanic plate; Black; Large strike-slip earthquakes in continental crust. Some historical earthquakes are shown with open triangles for comparison. Historical earthquakes (triangles) are keyed to Table 5.

is determined by integrating over the entire duration of the P wave, about 40 s, while the m_B determination is from a single pulse with a duration of only about 3 s. One possible reason for this good agreement is that the large coefficient, 2.4, for m_B in eq. (2) reflects some implicit scaling relation between the amplitude and the duration. Although Gutenberg and Richter determined this coefficient empirically, the commonly used ω-squared scaling relation (Aki 1967; Brune 1970) provides a partial explanation.

With a constant stress parameter and ω-squared spectrum, the spectral amplitude, a, is proportional to $M_0^{1/3}$ at frequencies much

Table 2. Some notable earthquakes.

Category	Key	Event	Year	Month	Day	Depth	M_w	m_B	T_p	n	C_m	E_{R_B}	ε_{R_B}	σ_{a_B}
Tsunami	A1	Nicaragua	1992	9	2	15	7.62	6.64	5.16	15	0.99	5.54E + 14	1.63E−06	7.18E−02
	A2	Java	1994	6	2	15	7.75	6.73	5.27	36	0.99	8.95E + 14	1.68E−06	7.40E−02
	A3	Peru	1996	2	21	15	7.5	6.7	4.36	28	0.98	7.76E + 14	3.48E−06	1.53E−01
	A4	Java	2006	7	17	20	7.71	6.79	3.91	56	0.87	1.21E + 15	2.63E−06	1.50E−01
	A5	Mentawai	2010	10	25	12	7.82	7.01	3.97	56	0.93	4.30E + 15	6.35E−06	2.52E−01
	A6	Central America	2012	8	27	12	7.34	6.62	5.03	56	0.86	4.74E + 14	3.74E−06	1.49E−01
Intraplate	B1	Mariana	1990	4	5	15	7.41	7.65	4.75	10	−0.8	1.48E + 17	9.07E−04	4.00E + 01
	B2	Kuril	1994	10	4	68.2	8.25	8.04	3.78	45	0.27	1.23E + 18	4.11E−04	2.78E + 01
	B3	Loyalty Islands	1995	5	16	24.7	7.66	7.82	4.31	23	−0.9	3.74E + 17	9.59E−04	6.53E + 01
	B4	Tonga	2006	5	3	67.8	7.97	7.79	4.17	42	0.63	3.17E + 17	2.83E−04	1.91E + 01
	B5	Kuril	2007	1	13	12	8.1	7.81	3.83	80	−0.6	3.44E + 17	1.94E−04	7.70E + 00
	B6	Samoa	2009	9	29	12	8.08	7.73	4.78	54	−0.54	2.26E + 17	1.36E−04	5.40E + 00
	B7	Chile[a]	2010	2	27	19.9	7.36	7.64	5.37	45	−0.87	1.35E + 17	9.88E−04	5.60E + 01
	B8	Sanriku[b]	2011	3	11	21.1	7.59	7.39	3.32	81	−0.89	3.40E + 16	1.10E−04	7.48E + 00
	B9	Kermadec	2011	7	6	22.3	7.58	7.5	3.9	36	−0.73	6.31E + 16	2.11E−04	1.33E + 01
	B10	Kermadec	2011	10	21	48.4	7.38	7.36	3.44	35	0.92	2.85E + 16	1.92E−04	1.30E + 01
	B11	Philippines	2012	8	31	45.2	7.62	7.68	3.86	57	0.74	1.70E + 17	5.03E−04	3.42E + 01
	B12	Sanriku[c]	2012	12	7	57.8	7.2	7.56	3.79	82	0.47	8.69E + 16	1.10E−03	7.46E + 01
	B13	Mexico	2017	9	8	44.8	8.23	7.77	4.06	51	−0.87	2.87E + 17	1.02E−04	6.89E + 00
Megathrust	C1	Peru	2001	6	23	29.6	8.38	7.63	4.32	34	0.7	1.29E + 17	2.76E−05	1.88E + 00
	C2	Sumatra	2004	12	26	28.6	9	7.87	4.33	60	0.78	4.93E + 17	1.25E−05	8.49E−01
	C3	Nias	2005	3	28	25.8	8.61	7.87	4.36	56	0.69	4.90E + 17	4.67E−05	3.18E + 00
	C4	Kuril	2006	11	15	13.5	8.3	7.53	5.15	80	0.98	7.49E + 16	2.13E−05	8.95E−01
	C5	Sumatra	2007	9	12	24.4	8.48	7.75	4.35	59	0.73	2.58E + 17	3.85E−05	2.62E + 00
	C6	Chile	2010	2	27	23.2	8.78	7.91	4.01	46	0.71	6.18E + 17	3.33E−05	2.17E + 00
	C7	Tohoku	2011	3	11	20	9.08	7.97	5.04	80	0.98	8.33E + 17	1.57E−05	8.92E−01
	C8	Chile	2014	4	1	21.6	8.12	7.73	4.83	54	0.82	2.26E + 17	1.19E−04	7.27E + 00
	C9	Nepal	2015	4	25	12	7.88	7.43	3.65	63	0.93	4.26E + 16	5.08E−05	2.02E + 00
	C10	Chile	2015	9	16	17.4	8.27	7.67	4.42	54	0.79	1.59E + 17	4.92E−05	2.47E + 00
Oceanic plate	D1	Indian Ocean	2000	6	18	15	7.87	7.56	3.91	58	−0.06	8.99E + 16	1.14E−04	5.01E + 00
	D2	Indian Ocean	2012	4	11	45.6	8.57	7.95	4.01	66	0.06	7.67E + 17	8.39E−05	5.70E + 00
	D3	Indian Ocean	2012	4	11	54.7	8.24	7.77	4.16	65	−0.03	2.79E + 17	9.64E−05	6.53E + 00
	D4	Indian Ocean	2016	3	2	37.2	7.78	7.57	3.69	66	0	9.14E + 16	1.54E−04	1.05E + 01
Strike-slip	E1	Izmit	1999	8	17	17	7.57	7.08	4.14	51	0.03	6.03E + 15	2.09E−05	1.03E + 00
	E2	Kunlun	2001	11	14	15	7.78	6.99	4.39	59	−0.13	3.79E + 15	6.42E−06	2.83E−01
	E3	Denali	2002	11	3	15	7.85	7.38	3.54	81	0.1	3.27E + 16	4.37E−05	1.93E + 00
	E4	Craig	2013	1	5	13.8	7.53	7.16	3.89	78	0.01	9.75E + 15	3.95E−05	1.67E + 00
	E5	Russia	2017	7	17	23.2	7.76	7.2	3.94	92	−0.02	1.23E + 16	2.27E−05	1.48E + 00
Intermediate	F1	Fiji	1997	10	14	165.9	7.7	7.31	3.88	24	−0.33	2.16E + 16	4.81E−05	3.19E + 00
	F2	Chile	2005	6	13	94.5	7.75	7.69	3.94	46	−0.9	1.81E + 17	3.41E−04	2.29E + 01
	F3	Fiji	2007	12	9	149.9	7.83	7.48	3.56	35	0.42	5.71E + 16	8.05E−05	5.36E + 00
	F4	Aleutian	2014	6	23	104.3	7.92	7.64	3.96	92	−0.14	1.39E + 17	1.43E−04	9.60E + 00
	F5	Mariana	2016	7	29	208.9	7.72	7.34	3.5	59	0.53	2.64E + 16	5.56E−05	3.99E + 00
	F6	Solomon Islands	2017	1	22	149.6	7.89	7.68	4.27	52	0.9	1.69E + 17	1.96E−04	1.30E + 01
Deep-focus	G1	Tonga	1994	3	9	567.8	7.59	7.16	3.42	27	−0.33	9.64E + 15	3.14E−05	3.63E + 00
	G2	Bolivia	1994	6	9	647.1	8.21	7.65	2.78	22	−0.67	1.45E + 17	5.53E−05	7.96E + 00
	G3	Flores_Sea	1996	6	17	584.2	7.84	7.23	2.92	41	−0.54	1.43E + 16	1.95E−05	2.32E + 00
	G4	Fiji	2002	8	19	630.9	7.63	7.54	2.96	37	−0.43	8.05E + 16	2.33E−04	3.17E + 01
	G5	Fiji	2002	8	19	699.3	7.69	7.51	3.27	37	0.92	6.59E + 16	1.55E−04	2.48E + 01
	G6	Okhotsk	2008	7	5	610.8	7.7	7.06	2.94	93	−0.51	5.58E + 15	1.25E−05	1.58E + 00
	G7	Mindanao	2010	7	23	576.9	7.64	7.11	2.94	53	−0.42	7.23E + 15	1.98E−05	2.33E + 00
	G8	Okhotsk	2012	8	14	598.2	7.72	7.07	2.81	88	0.66	5.73E + 15	1.19E−05	1.43E + 00
	G9	Okhotsk	2013	5	24	611	8.33	7.69	2.99	90	−0.97	1.76E + 17	4.47E−05	5.66E + 00
	G10	Bonin	2015	5	30	680.7	7.86	7.37	2.81	67	−0.43	3.13E + 16	4.09E−05	6.42E + 00
	G11	Peru-Brazil	2015	11	24	610.7	7.55	6.94	2.91	53	−0.89	2.89E + 15	1.10E−05	1.39E + 00
	G12	Peru-Brazil	2015	11	24	627.3	7.65	6.99	3.05	52	−0.9	3.81E + 15	1.03E−05	1.38E + 00
Other	H1	Taiwan	1999	9	20	21.2	7.62	7.39	4.17	50	0.93	3.51E + 16	1.04E−04	6.23E + 00
	H2	New Britain	2000	11	17	17	7.77	6.83	3.87	43	0.71	1.54E + 15	2.73E−06	1.34E-01
	H3	India	2001	1	26	19.8	7.62	7.71	4.36	59	0.49	1.98E + 17	5.77E−04	3.26E + 01
	H4	China	2008	5	12	12.8	7.9	7.55	4.13	61	0.47	8.32E + 16	9.27E−05	3.79E + 00
	H5	Haiti	2010	1	12	12	7.03	7.2	4.36	65	0.23	1.23E + 16	2.80E−04	1.11E + 01
	H6	Okhotsk	2013	5	24	642.4	6.73	6.85	2.09	96	−0.74	1.72E + 15	1.10E−04	1.56E + 01

[a]This event occurred about 86 min after the $M_w = 8.8$ Maule earthquake and the *P*-wave train is slightly perturbed by long-period coda.

[b]This event occurred about 39 min after the $M_w = 9.1$ Tohoku earthquake and the *P*-wave train is perturbed by long-period coda. T_p was measured after a high-pass filter at 0.167 Hz was applied to the *P*-wave train.

[c]This event is a doublet, one with normal faulting and the other with thrust, occurring within about 12 s, and the *P* waves from the two events overlap.

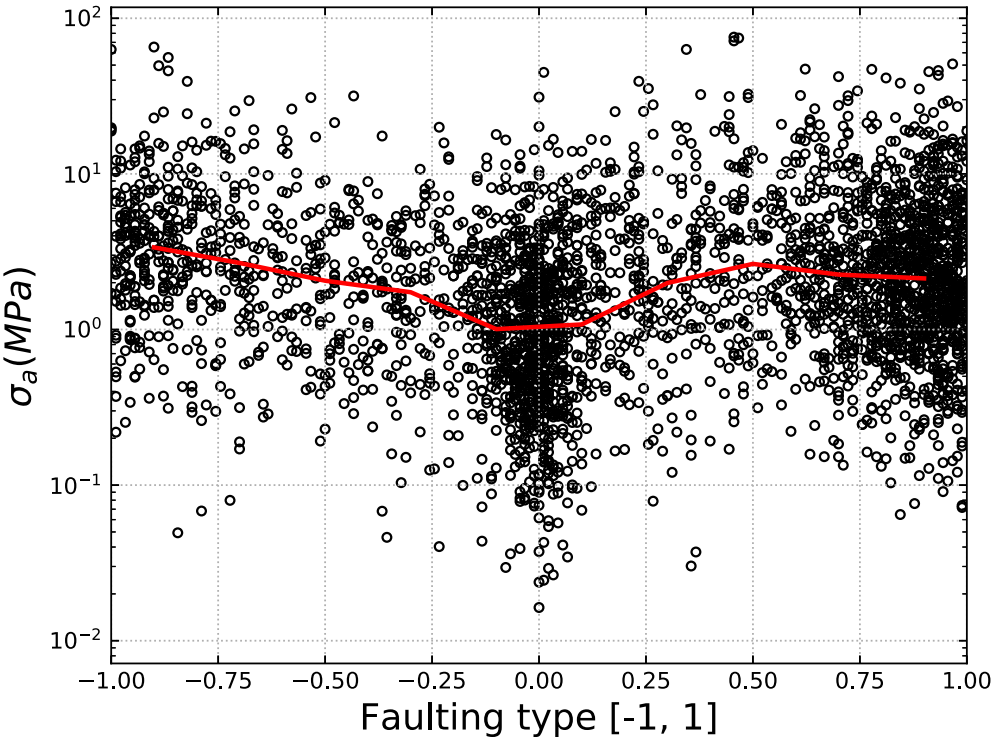

Figure 4. Variation of the apparent stress σ_{a_B} for different earthquake mechanisms. The horizontal axis is a simple scalar constant, C_m, which roughly represents the mechanism type (Shearer *et al.* 2006). $C_m = 1.0, 0.0, -1.0$ approximately indicate thrust (or reverse), strike-slip and normal fault earthquakes, respectively. The red curve indicates the median.

higher than the corner frequency (e.g. fig. 3 of Aki 1967). If we assume that the spectral amplitude is proportional to the time-domain amplitude, this relation leads to $m_B = 0.5M_w +$ constant. The coefficient 0.5 agrees with the slope of m_B versus M_w relation shown in Fig. 1 at large M_w, but is smaller than the overall trend. The difference could be due to other factors such as the difference in the spectral amplitude and the time-domain amplitude, and the increase of the corner frequency with decreasing M_w. The ω-squared spectrum results in $E_R \propto M_0$ if the stress parameter is constant (Madariaga 2009). This leads to $E_R \propto 10^{1.5M_W} \propto 10^{3m_B}$ which gives some support for the large coefficient 2.4 in eq. (2). Of course, the scaling relation is valid only on average, and we cannot expect it to hold for individual events.

The relationship for shallow events (Fig. 2a) is even more surprising, because the *P* wave train extends to 100–600 s for great earthquakes, yet, a single pulse with a period of only 3 s appears to represent the total energy reasonably well. Of course, we do not mean that m_B can replace the E_R measurements, but the comparison shown in Figs 2(a) and (b) is what we see in the data presently available, and the good agreement may not be entirely surprising after all, given the commonly accepted scaling relations in seismology. However, where the absolute energy is an issue, the difference shown in Fig. 2(a) and Fig. S1 of the Supporting Information must be accounted for. We include further discussion on this issue in the Appendix B

Notable features

We show some notable features revealed by the m_B measurements. Table 2 lists the events used in this and following sections. The event numbers in the figures are keyed to those in the table. The choice of the events is mainly for illustration purposes and is not necessarily systematic.

Scaled energy, $\varepsilon_R = (E_R/M_0)$

The moment scaled energy $\varepsilon_R = (E_R/M_0)$ is closely related to the apparent stress, $\sigma_a = \mu(E_R/M_0)(\mu$: rigidity) defined by Wyss & Brune (1968) and is a useful energy-related parameter for studying the global diversity of earthquake characteristics. For example, as shown by Newman & Okal (1998), Lay *et al.* (2012), and Ye *et al.* (2016b), ε_R can be effectively used for distinguishing large intraplate, megathrust and tsunami earthquakes.

Figs 3(a) and (b) show the ε_{R_B} versus M_w relation for events with $M_w \geq 6$ and $M_w \geq 7$, respectively. On average, ε_{R_B} is relatively constant over the large M_w range from 6 to 8 with a slight increasing trend with M_w. In Fig. 3(b) some known intraplate, tsunami, megathrust, strike-slip and intermediate and deep earthquakes are marked by different colours. In general, the pattern is similar to that seen in the published ε_R versus M_w diagrams, demonstrating that m_B or ε_{R_B} is a useful parameter for further investigation of the global diversity of earthquakes using the extended data base including old earthquakes. We will show some examples in a later section.

Apparent stress σ_{a_B} versus mechanism

Fig. 4 shows the variation of the apparent stress σ_{a_B} with the source mechanism. Here the source mechanism type is represented by a simple scalar parameter C_m used by Shearer *et al.* (2006) based mainly on the rake angle. $C_m = -1.0$, 0.0 and 1.0 roughly represent normal-fault, strike-slip and reverse-fault events, respectively. The dependence of σ_{a_B} on the mechanism type is weak, with slightly

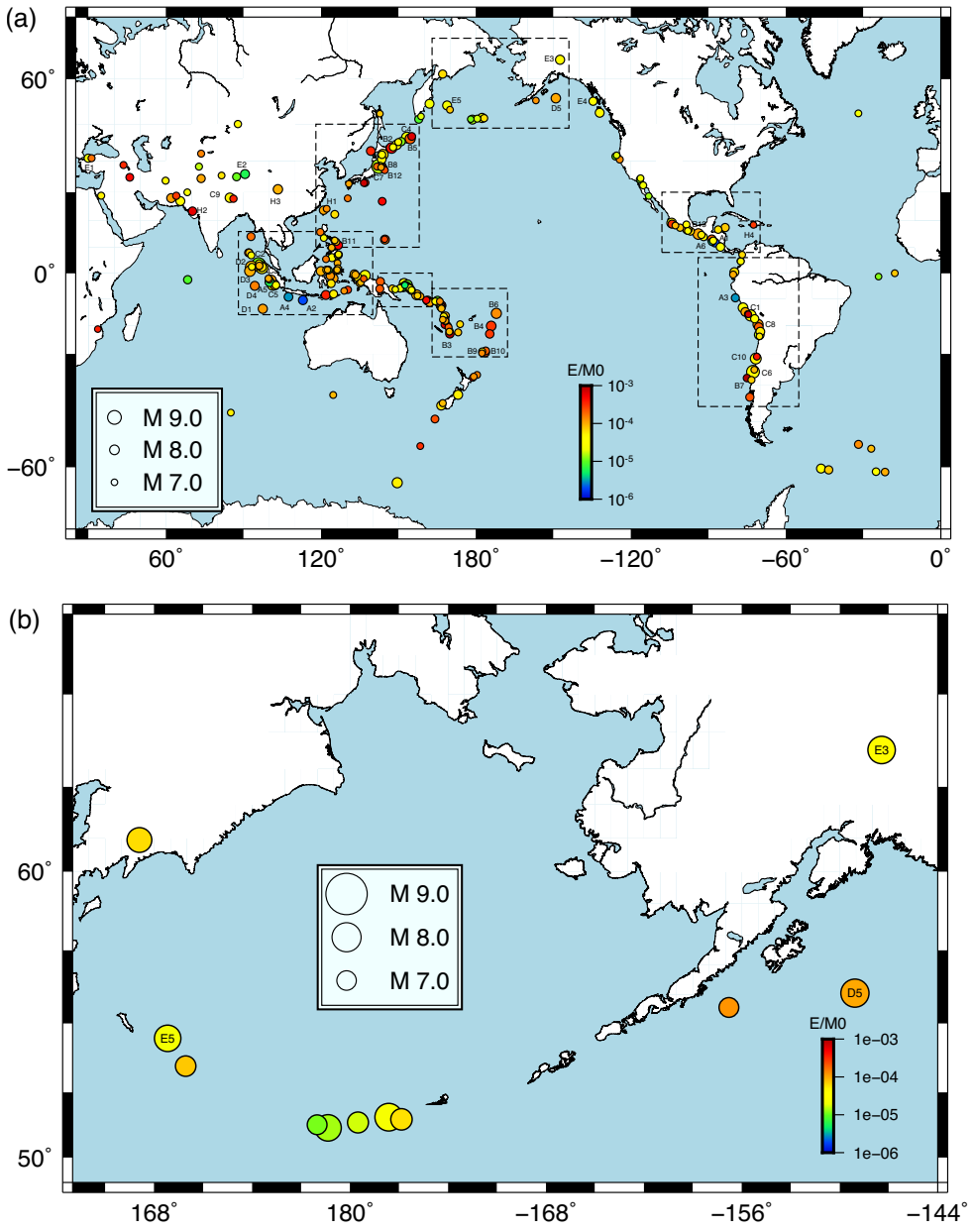

Figure 5. (a) Spatial distribution of scaled energy (E_{R_B}/M_0) for $M_w \geq 7$ earthquakes with depth $\leq$70 km. Some notable events are keyed to the list in Table 1. Details are in the boxed regions shown in Figs (b)–(h).

smaller values for strike-slip events. This pattern may be simply due to the proximity of teleseismic stations to *P*-wave radiation node for strike-slip events rather than the special physical property of strike-slip events. Allowing for the average difference in the radiation pattern between dip-slip and strike-slip events may reduce the difference, or even reverse the trend.

Spatial distribution of ε_{R_B}

Earthquakes with depth $\leq$*60 km* ($M_w \geq$ *7.0)* Fig. 5(a) shows the spatial distribution of scaled energy ε_{R_B} for $M_w \geq 7.0$ events on a global scale and Figs 5(b)–(h) show the regional distributions. Fig. 5 includes the events to a depth of 70 km. Notable features are: (i) Low ε_{R_B} values (blue) for known tsunami earthquakes [1992 Nicaragua (A1), 1994 Java (A2), 1996 Peru (A3), 2006 Java (A4), 2010 Mentawai (A5) and 2012 Central America (A6)]. Event H2 (Figs 3b and f) is a large event in the New Britain islands. This event is mentioned in Convers & Newman (2011) as a slow event and has a low ε_R value. (ii) High ε_{R_B} values (red and orange) for large lithospheric earthquakes [1990 Mariana (B1), 1994 Kuril (B2), 1995 Loyalty Is. (B3), 2006 Tonga (B4), 2007 Kuril (B5), 2009 Samoa (B-6), 2019 Chile (B7), 2011 Sanriku (B8), 2011 Kermadec (B9, B10), 2012 Philippines (B11), 2012 Sanriku (B12) and 2017 Mexico (B13)]. Here, we use the term lithospheric earthquakes for large events that occur in the subducting oceanic plate at depths shallower than 100 km. Some are normal-faulting, and others are thrust or oblique-faulting earthquakes. (iii) Intermediate to low ε_{R_B} values (yellow to green) for most large megathrust earthquakes [2001 Peru (C1), 2004 Sumatra (C2), 2005 Nias (C3), 2006 Kuril (C4), 2007 Sumatra (C5), 2010 Chile (C6), 2011 Tohoku (C7), 2014 Chile

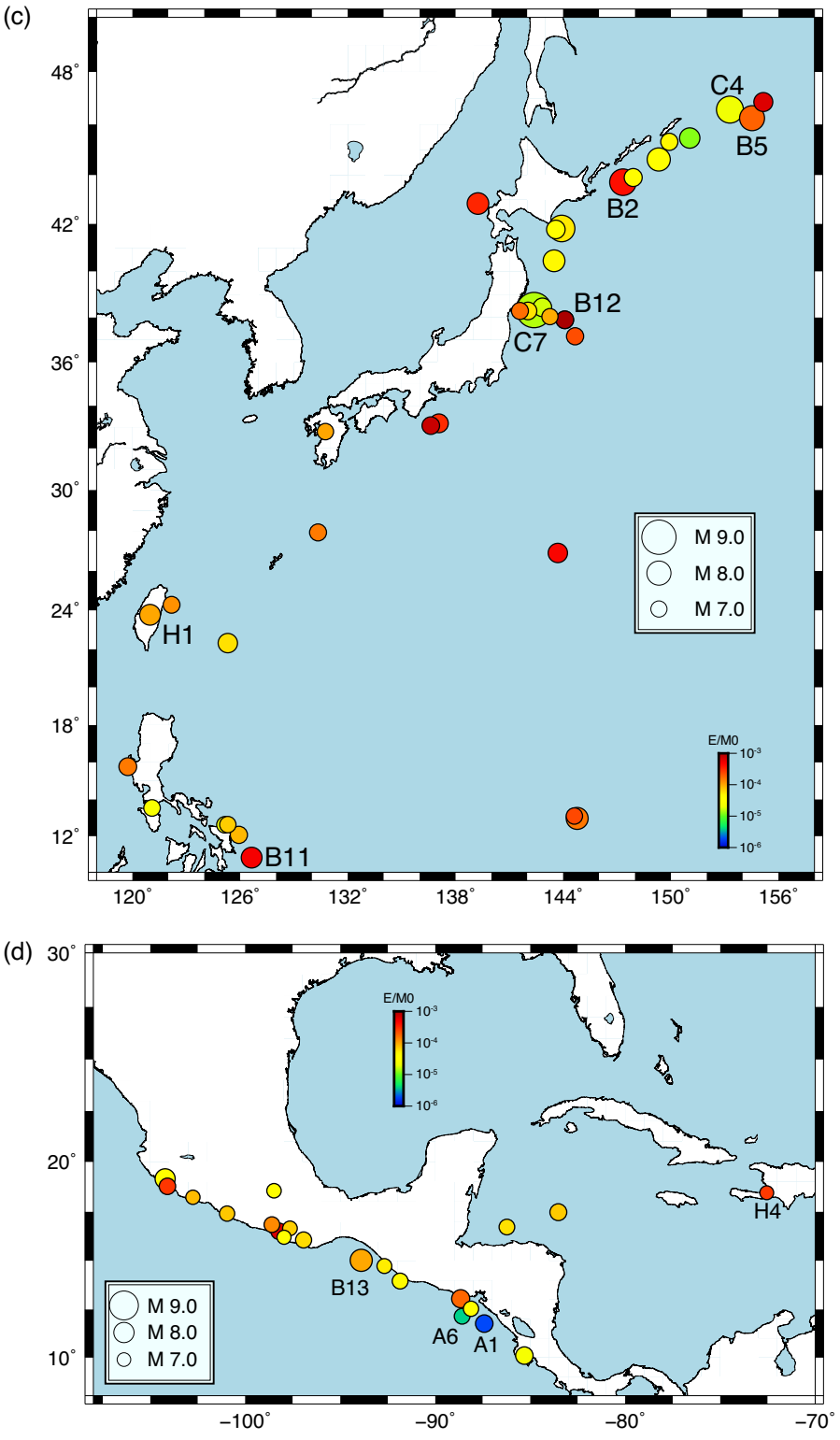

Figure 5. (*Continued.*)

(C8), 2015 Nepal (C9), 2015 Chile (C10)]. Notable exceptions are the 2014 Chile (C8) and the 2016 South Chile earthquakes. (iv) Relatively large ε_{R_B} values (orange) for large strike-slip earthquakes in the oceanic plate [2000 Indian Ocean (D1), 2012 Indian Ocean (D2, D3), 2016 Indian Ocean (D4), 2018 Alaska (D-5)]. (v) Variable ε_{R_B} values for large strike-slip earthquakes [1999 Izmit (E1), 2001 Kunlun (E2), 2002 Denali (E3), 2013 Craig (E4), and 2017 Russia (E5)].

Earthquakes with 60 km ≤ depth ≤ 300 km ($M_w \geq 7.0$) Fig. 6 shows the spatial distribution of ε_{R_B} for the intermediate-depth events with $M_w \geq 7$. Fig. 6 includes events from a depth of 50 km with a 20 km

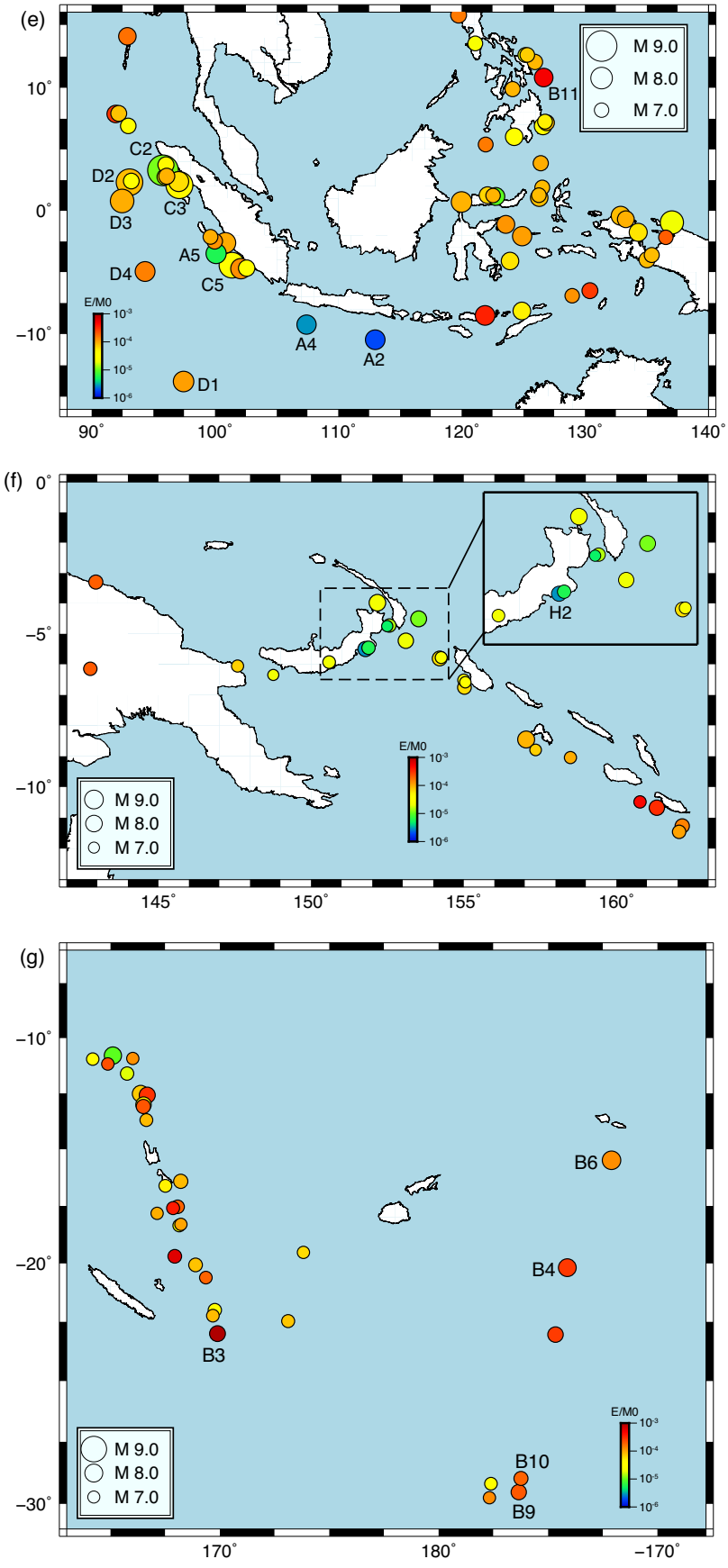

Figure 5. (*Continued.*)

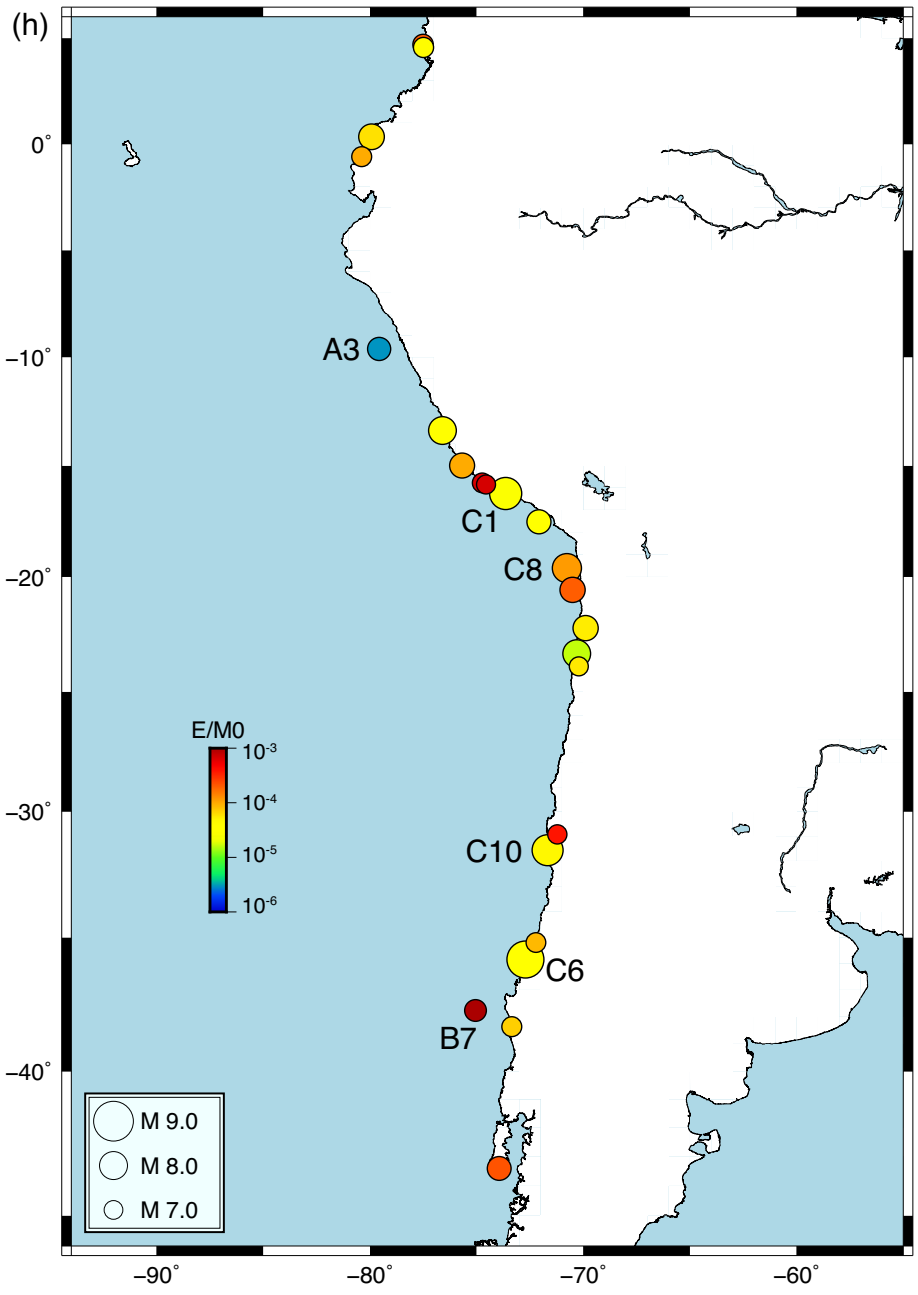

Figure 5. (*Continued.*)

overlapping depth range between Figs 5 and 6. A notable feature is that most large events at depths from 100 to 200 km have large ε_{R_B} values (red, orange), for example, 1997 Fiji (F1), 2005 Chile (F2), 2007 Fiji (F3), 2014 Aleutian Is. (F4), 2016 Mariana (F5) and 2017 Solomon Is. (F6).

Deep (depth ≥ 300 km) earthquakes ($M_w \geq 7.0$) Fig. 7 shows the spatial distribution of ε_{R_B} for deep events (depth ≥ 300 km) with $M_w \geq 7$. The two large events with large ε_{R_B} (G4 and G5) are the doublet studied by Tibi *et al.* (2003a).

Apparent stress, versus depth

Although the apparent stress σ_a itself does not represent a single unique physical property, it is a product of the seismic efficiency η and the average stress $\bar{\sigma}$ (Wyss & Brune 1968), and can be interpreted as the effective stress for energy radiation.

Fig. 8 shows $\sigma_{a\_B} = \mu(E_{R\_B}/M_0)$ as a function of depth where $\mu$is the rigidity at the centroid depth of the event. The rigidity used is taken from PREM (the rigidity values listed in PREM at discrete depth points are interpolated).

The solid red line indicates the median value in depth bins, while the dashed red line indicates the median overall depths. The overall pattern is similar to that shown in fig. 6.14B of Frohlich (2006).

Interesting observations include: (i) The large median σ_{a_B} at 50 to 200 km. The events with very large ε_{R_B} often seen in this depth range in several regions (Fig. 6) reflect this increased apparent stress level. (ii) Despite the increase in the overburden stress with depth, the apparent stress remains relatively constant with depth. In the group of very deep events with depth ≥500 km, large earthquakes

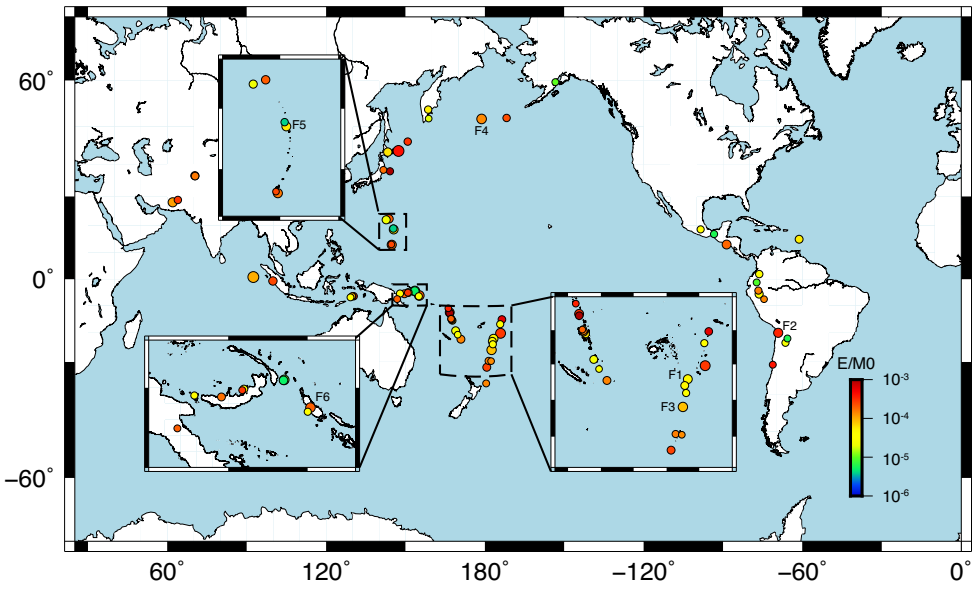

Figure 6. Spatial distribution of scaled energy (E_{R_B}/M_0) for $M_w \geq 7$ earthquakes with 50 km $\leq$ depth $\leq$ 300 km. Some notable events are keyed to the list in Table 1.

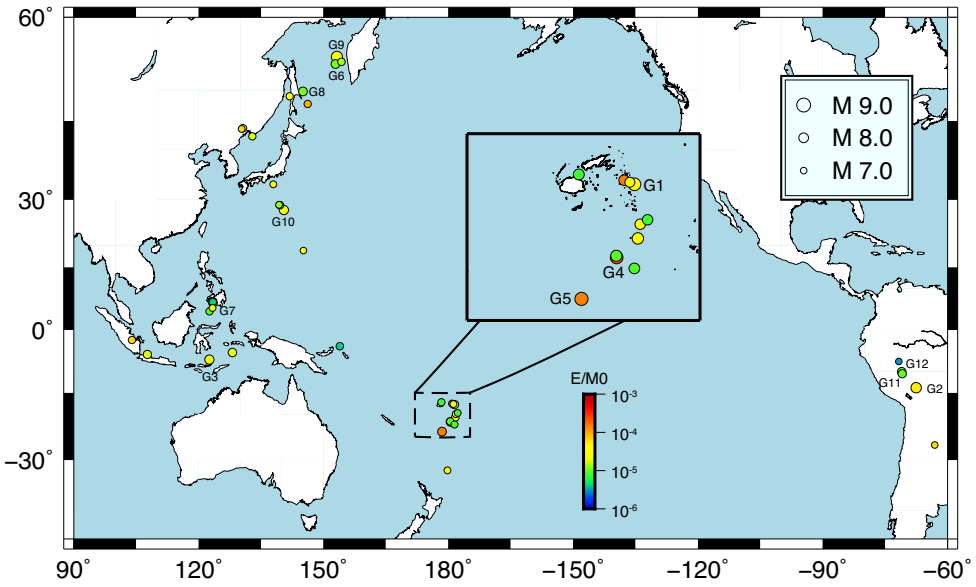

Figure 7. Spatial distribution of scaled energy (E_{R_B}/M_0) for $M_w \geq 7$ earthquakes with depth $\geq$300 km. Some notable events are keyed to the list in Table 1.

tend to have larger apparent stresses (G2, G4, G5 and G10). It is possible that as the events exceed a certain magnitude threshold, a runaway process may take over driving large slip (e.g. McGuire & Beroza 2012; Zhan 2017). (iii) The supershear deep event (H6 in Fig. 8, Zhan *et al.* 2015) has a large σ_{a_B}(∼15 MPa) for the relatively small M_w, 6.7.

As mentioned above, since the apparent stress is the product of efficiency and average stress, we cannot determine the physical mechanism of the events uniquely. Large σ_a can mean either large efficiency, large average stress or both, and the events with a similar σ_a may involve very different physical processes. For example, the 1994 Bolivia earthquake (G2, $M_w = 8.2$, depth = 637 km) and the 2013 Okhotsk event (G9, $M_w = 8.3$, depth = 598 km) have about the same σ_a, yet these two events may have very different physical mechanisms (e.g. Zhan *et al.* 2014).

Another caveat is that although Gutenberg & Richter determined the Q functions with large amounts of data considering the attenuation and geometrical spreading (Richter 1958, page 347–348), the database must have been sparser for deep events than shallow events, and the Q functions for different depths may not be completely mutually consistent.

RELATED OBSERVATIONS

Comparison of m_B and m_b

Abe's (1981) catalogue includes m_B values for most large shallow events for the period from 1904 to 1969 and for large intermediate and deep earthquakes for the period from 1904 to 1974. These values were mainly derived from Gutenberg's handwritten notepad

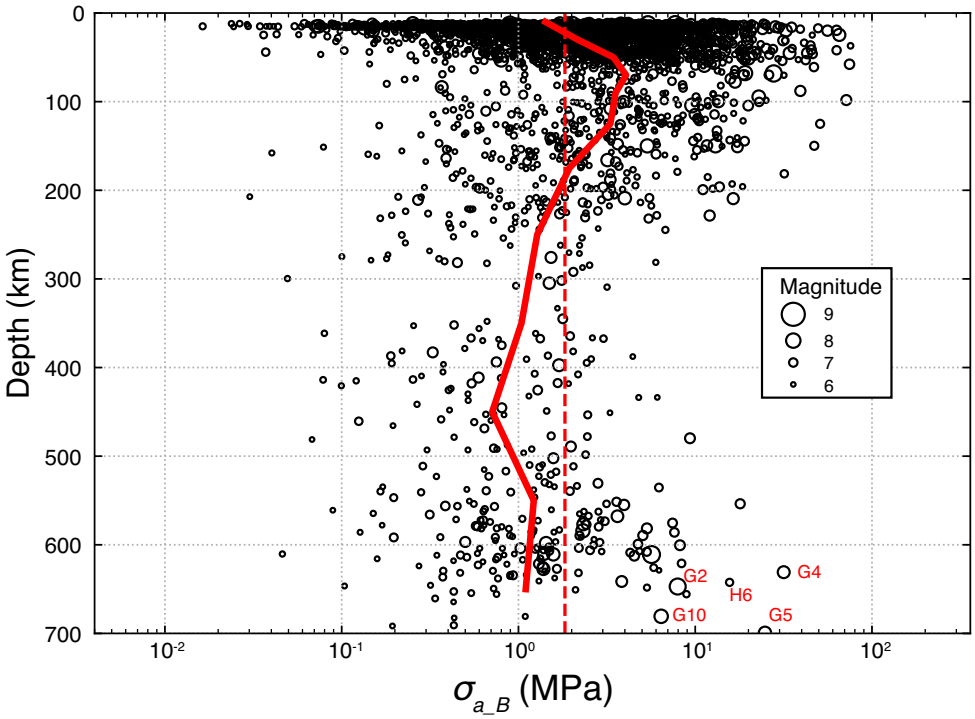

Figure 8. The apparent stress σ_{a_B} as a function of depth. For computation of σ_{a_B} the rigidity at the centroid depth of the event listed in the Global Centroid Moment Tensor (GCMT) catalogue is used. The solid red line indicates the median value in depth bins, while the dashed red line indicates the median overall depths.

Table 3. Body wave magnitude determined with different filters.

	M_w	$m_B^{3.5}$	m_B^{10}	0.9–1.3[a]	0.7–1.1[b]	0.5–0.9[c]	0.3–0.7[d]	0.1–0.5[e]	NEIC *mb*
2006 Java	7.7	6.79(3.93)[f]	6.85(9.37)	5.78(1.00)	6.00(1.25)	6.24(1.72)	6.56(2.53)	6.87(5.40)	6.1
2006 Kuril	8.3	7.52(4.80)	7.66(10.15)	6.30(1.01)	6.55(1.23)	6.75(1.70)	7.05(2.66)	7.57(6.84)	6.5
2011 Tohoku	9.1	8.05(4.57)	8.21(11.7)	7.04(0.99)	7.20(1.26)	7.38(1.66)	7.60(2.63)	7.98(7.15)	7.2
2012 Indian Ocean	8.6	7.95(3.89)	8.01(7.90)	6.88(1.01)	7.15(1.25)	7.36(1.71)	7.69(2.63)	8.02(5.72)	7.4
2018 G. Alaska	7.9	7.59(3.78)	7.70(7.39)	6.53(1.01)	6.80(1.26)	7.05(1.71)	7.34(2.63)	7.72(6.15)	7.0

[a]0.9–1.3: m_b determined with a bandpass filter at 0.9 to 1.3 Hz.
[b-e]Similar to [a]
[f]Number in parentheses is period in seconds.

[the backup material for Gutenberg & Richter's (1954) Seismicity of the Earth; Goodstein *et al.* 1980] and Abe's own determinations. Other catalogues that list m_B include Abe and Kanamori (1980) and Engdahl & Villaseñor (2002). For other periods, the availability of m_B is limited. Since the end of the 1960s, with evolving interest in monitoring nuclear explosions, a short-period body wave magnitude m_b has been determined. Although the details of the method (filter response, window length of the *P*-wave train used etc.) changed considerably with time, the reported magnitude has been generally listed as m_b (Granville *et al.* 2005; Di Giacomo *et al.* 2015). In some cases (e.g. Houston & Kanamori 1986; Kanamori 2006) m_b measured over an extended *P*-wave time window was labelled as $\hat{m}_b$. These magnitudes are all measured from relatively narrowband records at a period of around 1 s, and cannot be directly compared with m_B.

To utilize m_b for general seismological research, we try to relate m_B to m_b using the waveform data we have assembled. Since the details of m_b determinations varied in time, we try to replicate m_b listed in the recent NEIC catalogue using our method. We first try a WWSSN SP (short-period) response for the filter to determine the magnitude of a few representative events and compare them with m_b listed in the NEIC catalogue. The agreement is generally satisfactory, but we find that if we use a narrow bandpass filter from 0.7 to 1.1 Hz (here denoted by $m_b{}^{f\_0.7-1.1}$), we can best replicate the NEIC results (as shown in Table 3). We compute $m_b{}^{f\_0.7-1.1}$ for all the events with $M_w \geq 6$ for the period 1988–present using the waveform database used in this study. Fig. 9 shows the difference $m_B{}^{3.5} - m_b{}^{f\_0.7-1.1}$ as a function of M_w. The average difference is about 0.7 m_B unit and is independent of M_w. However, some large deep events, like the 2013 Okhotsk (G9, $M_w = 8.3$), 1994 Bolivia (G2, $M_w = 8.2$) and the 2015 Bonin Is. (G10, $M_w = 7.9$) earthquakes, tend to have somewhat smaller differences, 0.3 to 0.45, because of the strong high-frequency excitation of deep earthquakes. For a few events we also compare m_B in this paper with $\hat{m}_b$ determined by Houston & Kanamori (1986) and Kanamori (2006). As shown in Table 4, the average difference $m_B - \hat{m}_b$ is approximately 0.7, the same as $m_B{}^{3.5} - m_b{}^{f\_0.7-1.1}$. These calibrations allow us to compare recent events with old events without direct determination of m_B; however, some uncertainty due to the scatter in Fig. 9 is inevitable.

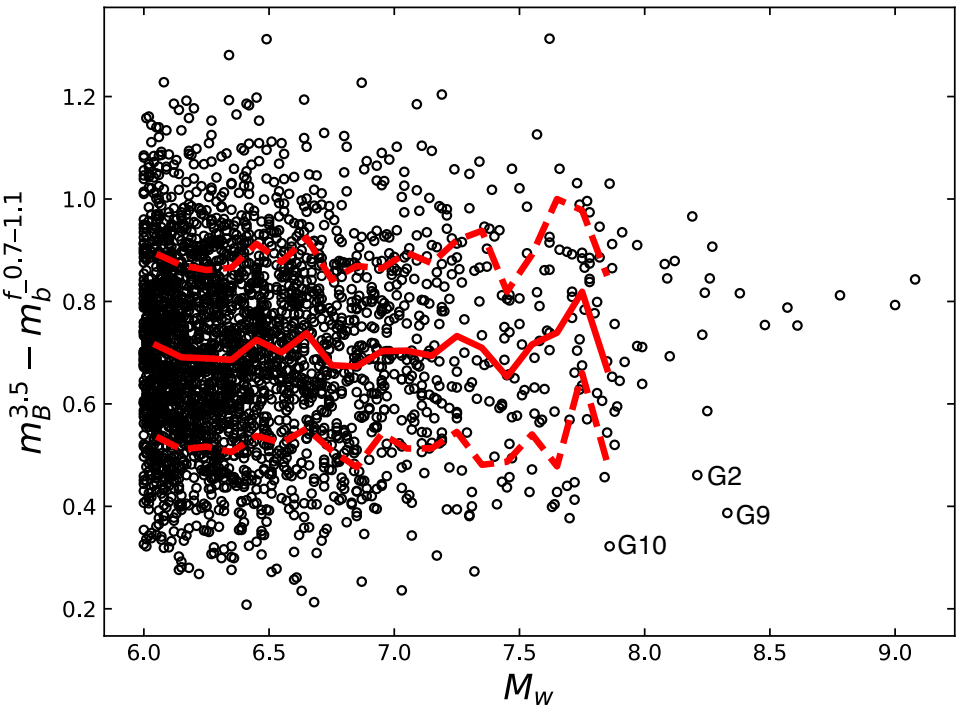

Figure 9. Difference $m_B^{3.5} - m_b^{f\_0.7-1.1}$ as a function of M_w where $m_B^{3.5}$ is m_B determined with a 3.5 s Wiechert seismograph (the same as m_B in this paper), and $m_b^{f\_0.7-1.1}$ is m_b determined with a narrow bandpass (0.7–1.1 Hz) filtered records. The average and ±1 standard deviations are shown by the red solid and dashed curves, respectively.

Table 4. Comparison of m_B and $\hat{m}_b$.

Event	M_w	m_B	$\hat{m}_b$	$m_B - \hat{m}_b$
1992 Nicaragua	7.6	6.64	5.74	0.90
2001 Peru	8.4	7.63	6.95	0.68
2003 Tokachi-Oki	8.3	7.68	6.85	0.83
2004 Sumatra	9.0	7.87	7.25	0.62
2005 Nias	8,6	7.87	7.26	0.61

m_B at different periods and the source spectrum

The method described here can be easily extended to any period. For example, because some old measurements of m_B were made at a longer period like 10 s, we compute m_B with a Wiechert response with $T_s = 10$ s ($m_B{}^{10}$) for a few representative events as shown in Table 3 and Fig. 10(a). The difference between $m_B{}^{3.5}$ and $m_B{}^{10}$ is small, usually less than 0.15. For more general comparison, we compute $m_B^{7.5}$ and plot the difference $m_B^{7.5} - m_B^{3.5}$ in Fig. 10(b). About 72 per cent of the events fall in the range from 0 to 0.1. The two outliers with a difference of >0.2 are the events following a larger event, and probably $m_B^{7.5}$ is badly perturbed.

We also compute m_b with several narrowband filters, 0.1 to 0.5, 0.3 to 0.7, 0.5 to 0.9, 0.7 to 1.1 and 0.9 to 1.3 Hz, and the results are shown in Table 3 and Fig. 10(a). Here we use m_b to denote the magnitude with a narrowband filter. The m_b values increase with period, but at periods longer than 4 s, the rate of change decreases. These figures can be roughly interpreted as the ground-motion velocity spectrum, or $f\,\dot{M}_0(f)$ where f is the frequency and $\dot{M}_0(f)$ is the moment-rate spectrum. For some spectral applications, the narrowband m_b can be useful.

The value of m_B with the 3.5 s Wiechert-type response is larger than m_b with the narrowband filter around 3.5 s (Fig. 10), because the Wiechert-type response has a broader bandwidth. Also, as mentioned above, m_B with the Wiechert-type response does not depend much on the period above 3.5 s. This is the reason why Gutenberg and Richter chose to use a single m_B to represent the total energy. This may not be the case for very large events, but for most earthquakes studied by Gutenberg and Richter, this was a reasonable practice.

Comparison of recent and old earthquakes

To compare m_B and M_w for recent and historical events, we must keep in mind the following issues. For most old events, accurate M_w is not known. The M_w values assigned to many old events are often a proxy M_w, the values empirically computed from other magnitudes. Also, it is important to know the distribution of the stations used for m_B determinations. This could be examined for individual events by checking Gutenberg's notepad together with historical seismograms, but it is not that straightforward. Thus, in this paper we show in Fig. 3(b) a few examples listed in Table 5 (historical events are keyed to Table 5). Ye *et al.* (2017) have already shown that ε_{R_B} for the two large lithospheric earthquakes, the 1931 Oaxaca (I6) and the 1933 Sanriku (I5) earthquakes, are consistent with those from recent events. The 1977 Sumba outer-rise normal-fault earthquake lies on the same trend. The 1906 San Francisco earthquake (I10) has nearly identical values of M_w and m_B to the 2002 Denali earthquake. For the 1946 Aleutian islands tsunami earthquake (I4), the result is consistent with that of Lopez and Okal (2006). For the two great megathrust earthquakes, the 1960 Chile and 1964 Alaska earthquakes, we show two values for ε_{R_B} with a large difference: one from m_B listed in Abe (1981) and the other from $\hat{m}_b$ listed in Houston & Kanamori (1986). For the 1964 Alaska earthquake, Kikuchi & Fukao (1988) reported a direct estimate of E_R

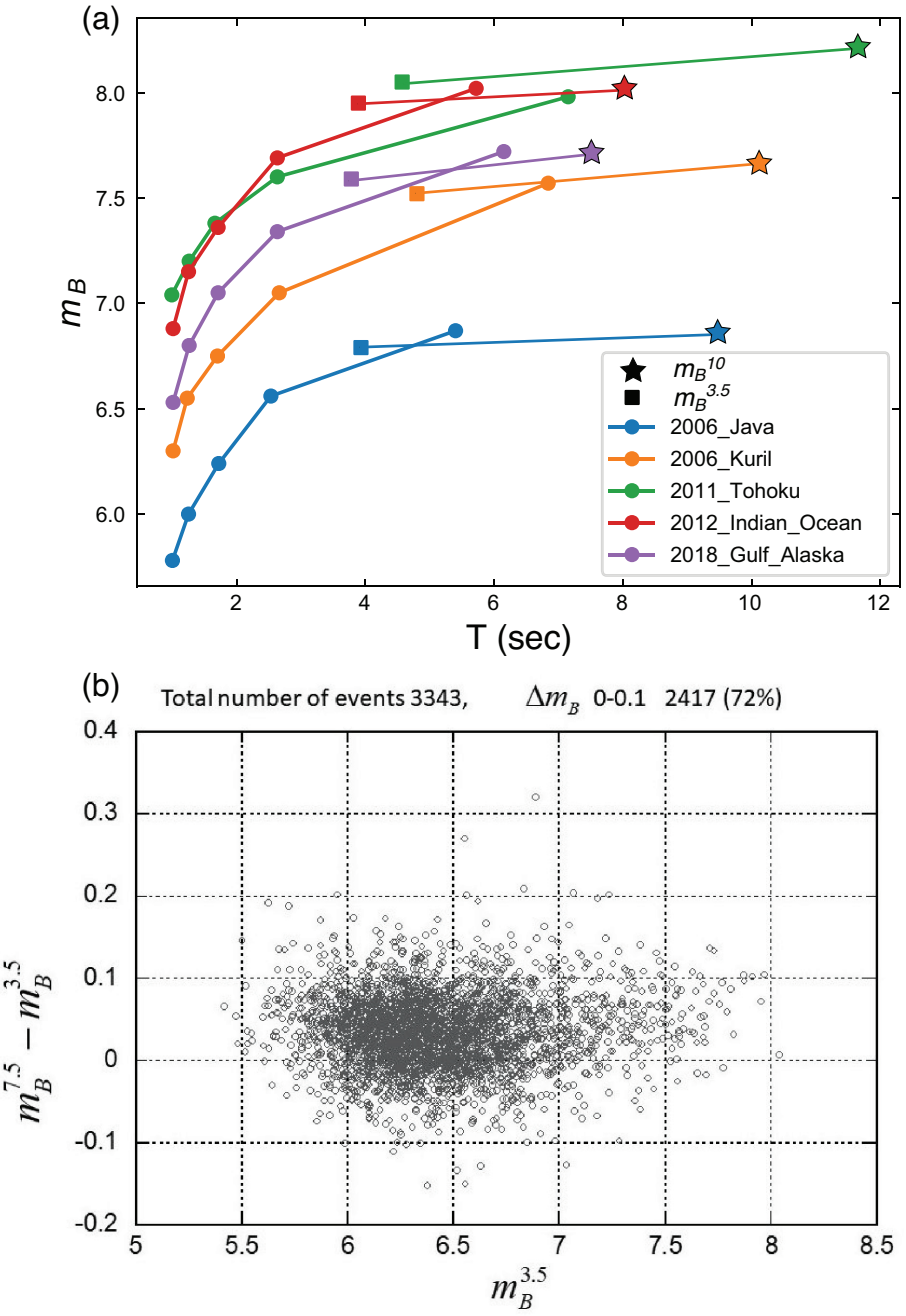

Figure 10. (a) m_b with narrow bandpass filters (0.9–1.3, 0.7–1.1, 0.5–0.9, 0.3–0.7 and 0.1–0.5 Hz). The square and star symbols indicate $m_B^{3.5}$, and m_B^{10}, respectively. (b) Difference $\Delta m_B = m_B^{7.5} - m_B^{3.5}$ versus $m_B^{3.5}$. Note that Δm_Bs of 72 per cent of the events fall within 0.0 and 0.1. The two outliers with the difference larger than 0.2 are events following a larger magnitude event. The *P* wave is disturbed by long-period coda of the preceding event, and m_B computed at 7.5 s is affected by the coda.

which is even smaller than E_{R_B} estimated from m_B. Unfortunately, the m_B data for the 1960 and 1964 events are not from Gutenberg's notepad, but from Abe's own measurements. Abe's original data are not presently available. In any case, it is unclear how m_B was measured for such large events, and we cannot confirm the result shown in Fig. 3(b) and further investigation is desirable. Another interesting case is for the 1906 Ecuador-Colombia earthquake (I8) which has a large ε_{R_B} comparable to that of lithospheric events. In general this event is believed to be a multiple megathrust event (e.g. Kanamori & McNally 1982; Ye *et al.* 2016a; Nocquet *et al.* 2017; Tsuzuki *et al.* 2017; Yoshimoto *et al.* 2017), but so far no explicit suggestion has been made concerning its possible association with lithospheric rupture. More detailed examinations of the m_B data and seismograms are needed to further investigate this question. Thus, comparison of m_B between old and recent events suggests an interesting line of investigation.

CONCLUSION

With the advent of modern broad-band seismic networks, we can compute the body wave magnitude m_B reliably and robustly for 3317 $M_w \geq 6$ earthquakes for the period from 1988 to the present.

Table 5. Some historical events.

Key	Event	M_w	m_B[a]	ε_{R_B}	$\hat{m}_b$[b]	$\varepsilon_{R\_B \text{ from } \hat{m}_b}$
I1	1960 Chile	9.5	7.9	2.9×10^{-6}	7.57	2.0×10^{-5}
I2	1964 Alaska	9.2	7.9	7.7×10^{-6}	7.64	8.2×10^{-5}
I3	1952 Kamchatka	9.0	7.9	1.5×10^{-5}	–	–
I4	1946 Aleutian	8.5[c]	7.2	1.4×10^{-6}	–	–
I5	1933 Sanriku	8.4	8.2[d]	6×10^{-4}	–	–
I6	1931 Oaxaca	7.5[e]	7.6	3×10^{-4}	–	–
I7	1977 Sumba	8.3[f]	–	–	7.47	7.2×10^{-4}
I8	1906 Ecuador-Colombia	8.6[g]	8.2	3×10^{-4}	–	–
I9	1970 Colombia	8.1[h]	7.5	3.7×10^{-5}	–	–
I10	1906 San Francisco	7.9	7.4	4×10^{-5}	–	–

[a]Geller & Kanamori (1977) and Abe (1981) unless otherwise noted.
[b]Houston and Kanamori (1986) and $m_B = \hat{m}_b + 0.7$
[c]Pelayo & Wiens (1992) and Lopez & Okal (2006)
[d]Kanamori (1971)
[e]Singh *et al.* (1985)
[f]Lynnes & Lay (1988)
[g]Estabrook (2004), Ye *et al.* (2016a), Tibi *et al.* (2003b)
[h]Estabrook (2004), Ye *et al.* (2016a), Tibi *et al.* (2003b)

Although m_B is a simple parameter, our calibration against the radiated energy, E_R, estimated for recent events with a modern practice suggests that the radiated energy, E_{R_B}, derived from m_B can be used as a good proxy for E_R for investigating the regional and depth variations of energy-related properties.

Since m_B and m_b data are available for old events since 1904, we can extend the database in time to investigate the diversity of global earthquakes. However, m_B is based on many simple assumptions and the Q functions were developed by Gutenberg and Richter nearly 80 yr ago; thus, caution must be exercised against overinterpretation. In most cases the results obtained with m_B can be best used to guide more detailed analysis with modern practice.

ACKNOWLEDGEMENTS

We thank James Dewey for providing us with helpful information on the practice for magnitude determination at the National Earthquake Information Center (NEIC) of the U.S. Geological Survey. Numerous discussions with him helped us to maintain the consistency of our results with the traditional m_b and m_B. We benefitted from discussion with Luis Rivera on spectral scaling relations. Comments from Lingling Ye and Thorne Lay resulted in clarification of the main points of this work. We thank Larry Ruff for a helpful review. We thank an anonymous reviewer for a very careful review of the manuscript and stimulating comments. We extensively used the continuous broad-band seismograms orderly archived at the Data Management Center of the Incorporated Research Institutions for Seismology (IRIS). We acknowledge the contributions of many global seismic networks that provided their data to the IRIS database. We used General Mapping Tools developed and maintained by Paul Wessel and Walter Smith. Z.E.R was supported by the Gordon and Betty Moore Foundation.

REFERENCES

Abe, K., 1981. Magnitudes of large shallow earthquakes from 1904 to 1980, *Phys. Earth planet. Inter.,* **27,** 72–92.

Abe, K., 1982. Magnitude, seismic moment and apparent stress for major deep earthquakes, *J. Phys. Earth,* **30,** 321–330.

Abe, K. & Kanamori, H., 1980. Magnitudes of great shallow earthquakes from 1953 to 1977, *Tectonophysics,* **62,** 191–203.

Aki, K., 1967. Scaling law of seismic spectrum, *J. geophys. Res.,* **72,** 1217–1231.

Baltay, A.S., Beroza, G.C. & Ide, S., 2014. Radiated energy of great earthquakes from teleseismic empirical Green's function deconvolution, *Pure appl. Geophys.,* **171,** 2841–2862.

Boatwright, J. & Choy, G.L., 1986. Teleseismic estimates of the energy radiated by shallow earthquakes, *J. geophys. Res.,* **91,** 2095–2112.

Bormann, P. & Saul, J., 2008. The new IASPEI standard broadband magnitude m B, *Seismol. Res. Lett.,* **79,** 698–705.

Bormann, P., Wendt, S. & Di Giacomo, D., 2013. Seismic sources and source parameters, in *New Manual of Seismological Observatory Practice 2 (NMSOP2),* p. 1–259, ed. Bormann, P., Deutsches GeoForschungsZentrum GFZ.

Brune, J.N., 1970. Tectonic stress and the spectra of seismic shear waves from earthquakes, *J. geophys. Res.,* **75,** 4997–5009.

Convers, J.A. & Newman, A.V., 2011. Global evaluation of large earthquake energy from 1997 through mid-2010, *J. geophys. Res.,* **116,** B08304, doi:10.1029/2010JB007928.

Di Giacomo, D. & Storchak, D.A., 2016. A scheme to set preferred magnitudes in the ISC Bulletin, *J. Seismol.,* **20,** 555–567.

Di Giacomo, D., Bondár, I., Storchak, D.A., Engdahl, E.R., Bormann, P. & Harris, J., 2015. ISC-GEM: Global Instrumental Earthquake Catalogue (1900–2009), III. Re-computed MS and m_b, proxy M_w, final magnitude composition and completeness assessment, *Phys. Earth planet. Inter.,* **239,** 33–47.

Duputel, Z., Tsai, V.C., Rivera, L. & Kanamori, H., 2013. Using centroid time-delays to characterize source durations and identify earthquakes with unique characteristics, *Earth planet. Sci. Lett.,* **374,** 92–100.

Dziewonski, A., Chou, T.A. & Woodhouse, J., 1981. Determination of earthquake source parameters from waveform data for studies of global and regional seismicity, *J. geophys. Res.,* **86,** 2825–2852.

Ekström, G., Nettles, M. & Dziewoński, A., 2012. The global CMT project 2004–2010: centroid-moment tensors for 13,017 earthquakes, *Phys. Earth planet. Inter.,* **200,** 1–9.

Engdahl, E.R. & Villaseñor, A., 2002. Global Seismicity: 1900–1999. In *International Geophysics,* p. 665–662, Elsevier.

Estabrook, C.H., 2004. Seismic constraints on mechanisms of deep earthquake rupture, *J. geophys. Res.,* **109,** B02306, doi: 10.1029/2003JB002449.

Frohlich, C., 2006. *Deep Earthquakes,* pp. 590, Cambridge Univ. Press, Cambridge.

Geller, R.J. & Kanamori, H., 1977. Magnitudes of great shallow earthquakes from 1904 to 1952, *Bull. seism. Soc. Am.,* **67,** 587–598.

Goodstein, J.R., Kanamori, H. & Lee, W., 1980. Seismology micrifiche publications from the Caltech Archive, *Bull. seism. Soc. Am.,* **70,** 657–658.

Granville, J.P., Richards, P.G., Kim, W.-Y. & Sykes, L.R., 2005. Understanding the differences between three teleseismic m_b scales, *Bull. seism. Soc. Am.,* **2005,** 1809–1824.

Gutenberg, B. & Richter, C.F., 1942. Earthquake magnitude, intensity, energy, and acceleration, *Bull. seism. Soc. Am.,* **32,** 163–191.

Gutenberg, B., 1945a. Amplitudes of *P*, *PP*, and *S* and magnitude of shallow earthquakes, *Bull. seism. Soc. Am.,* **35,** 57–69.

Gutenberg, B., 1945b. Magnitude determination of deep-focus earthquakes, *Bull. seism. Soc. Am.,* **35,** 117–130.

Gutenberg, B. & Richter, C., 1955. Magnitude and energy of earthquakes, *Nature,* **176,** 795.

Gutenberg, B. & Richter, C.F., 1956a. Magnitude and energy of earthquakes, *Ann. geofis.,* **9,** 1–15.

Gutenberg, B. & Richter, C.F., 1956b. Earthquake magnitude, intensity, energy, and acceleration: (second paper), *Bull. seism. Soc. Am.,* **46,** 105–145.

Gutenberg, B. & Richter, C.F., 1954. *Seismicity of the Earth and Related Phenomena,* pp. 310, Princeton University Press, Princeton.

Houston, H. & Kanamori, H., 1986. Source spectra of great earthquakes: teleseismic constraints on rupture process and strong motion, *Bull. seism. Soc. Am.,* **76,** 19–42.

IASPEI(2005). Summary of Magnitude Working Group recommendations on standard procedures for determining earthquake magnitudes from digital data, preliminary version October 2005,ftp://ftp.iaspei.org/pub/commissions/CSOI/summary_of_WG_recommendations_2005.pdf, last accessed June 2018.

IASPEI(2013). Summary of Magnitude Working Group recommendations on standard procedures for determining earthquake magnitudes from digital data, updated version 27 March 2013,ftp://ftp.iaspei.org/pub/commissions/CSOI/Summary_WG_recommendations_20130327.pdf, last accessed June 2018.

IRIS DMC, 2013. Data Services Products: EQEnergy Earthquake energy & rupture duration, doi:10.1785/0220160190.

Kanamori, H., 1971. Seismological evidence for a lithospheric normal faulting—the Sanriku earthquake of 1933, *Phys. Earth planet. Inter.,* **4,** 289–300.

Kanamori, H., 1983. Magnitude scale and quantification of earthquakes, *Tectonophysics,* **93,** 185–199.

Kanamori, H., 2005. Real-time seismology and earthquake damage mitigation, *Annu. Rev. Earth Planet. Sci.,* **33,** 195–214.

Kanamori, H., 2006. Seismological aspects of the December 2004 great Sumatra-Andaman earthquake, *Earthq. Spectra,* **22,** 1–12.

Kanamori, H., 2014. The diversity of large earthquakes and its implications for hazard mitigation, *Annu. Rev. Earth Planet. Sci.,* **42,** 7–26.

Kanamori, H. & McNally, K.C., 1982. Variable rupture mode of the subduction zone along the Ecuador-Colombia coast, *Bull. seism. Soc. Am.,* **72,** 1241–1253.

Kikuchi, M. & Fukao, Y., 1988. Seismic wave energy inferred from long-period body wave inversion, *Bull. seism. Soc. Am.,* **78,** 1707–1724.

Lay, T., Kanamori, H., Ammon, C.J., Koper, K.D., Hutko, A.R., Ye, L., Yue, H. & Rushing, T.M., 2012. Depth-varying rupture properties of subduction zone megathrust faults, *J. geophys. Res.,* 117, doi:10.1029/2011JB009133

López, A.M. & Okal, E.A., 2006. A seismological reassessment of the source of the 1946 Aleutian 'tsunami'earthquake, *Geophys. J. Int.,* **165,** 835–849.

Lynnes, C.S. & Lay, T., 1988. Source process of the great 1977 Sumba earthquake, *J. geophys. Res.,* **93,** 13 407–13 420.

Madariaga, R., 2009. Earthquake scaling laws, in *Encyclopedia of Complexity and Systems Science,* p. 2581–2600.

McGuire, J.J. & Beroza, G.C., 2012. A rogue earthquake off Sumatra, *Science,* **336,** 1118–1119.

Nakamura, Y., 1988. On the urgent earthquake detection and alarm system (UrEDAS), in *Ninth World Conf. Earthq . Eng.,* Tokyo.

Newman, A.V. & Okal, E.A., 1998. Teleseismic estimates of radiated seismic energy: the E/M 0 discriminant for tsunami earthquakes, *J. geophys. Res.,* **103,** 26 885–26 898.

Nocquet, J.-M. *et al.*, 2017. Supercycle at the Ecuadorian subduction zone revealed after the 2016 Pedernales earthquake, *Nat. Geosci.,* **10,** 145–149.

Okal, E.A., 2018. Energy and magnitude: a historical perspective, *Pure appl. Geophys.,* 1–35, doi:10.1007/s00024-018-1994-7.

Pelayo, A.M. & Wiens, D.A., 1992. Tsunami earthquakes: Slow thrust-faulting events in the accretionary wedge, *J. geophys. Res.,* **97,** 15 321–15 337.

Richter, C.F., 1958. *Elementary Seismology,* pp. 768, W. H. Freeman and Cooper.

Shearer, P.M., Prieto, G.A. & Hauksson, E., 2006. Comprehensive analysis of earthquake source spectra in southern California, *J. geophys. Res.,* **111,** doi:10.1029/2005JB003979.

Singh, S., Suárez, G. & Domínguez, T., 1985. The Oaxaca, Mexico, earthquake of 1931: lithospheric normal faulting in the subducted Cocos plate, *Nature,* **317,** 56–58.

Storchak, D., Di Giacomo, D., Engdahl, E., Harris, J., Bondár, I., Lee, W., Bormann, P. & Villaseñor, A., 2015. The ISC-GEM global instrumental earthquake catalogue (1900–2009): introduction, *Phys. Earth planet. Inter.,* **239,** 48–63.

Tibi, R., Wiens, D.A. & Inoue, H., 2003a. Remote triggering of deep earthquakes in the 2002 Tonga sequences, *Nature,* **424,** 921–925.

Tibi, R., Bock, G. & Wiens, D.A., 2003b. Source characteristics of large deep earthquakes: constraint on the faulting mechanism at great depths, *J. geophys. Res.,* **108,** 2091, doi:10.1029/2002JB001948, B2.

Tsuzuki, M., Koyama, J., Gusman, A.R. & Yomogida, K., 2017, Re-evaluation of earthquake and tsunami magnitudes of the 1906 Great Ecuador-Colombia earthquake, *J. Seismol. Soc. Japan,* **69,** 87–98.

Utsu, T., 2002. Relationships between magnitude scales, in *International Geophysics,* pp. 733–746, Elsevier.

Winslow, N.W. & Ruff, L.J., 1999. A hybrid method for calculating the radiated wave energy of deep earthquakes, *Phys. Earth planet. Inter.,* **115,** 181–190.

Wyss, M. & Brune, J.N., 1968. Seismic moment, stress, and source dimensions for earthquakes in the California-Nevada region, *J. geophys. Res.,* **73,** 4681–4694.

Ye, L., Kanamori, H., Avouac, J.-P., Li, L., Cheung, K.F. & Lay, T., 2016a. The 16 April 2016, M_w 7.8 (Ms 7.5) Ecuador earthquake: a quasi-repeat of the 1942 Ms 7.5 earthquake and partial re-rupture of the 1906 Ms 8.6 Colombia–Ecuador earthquake, *Earth planet. Sci. Lett.,* **454,** 248–258.

Ye, L., Lay, T., Kanamori, H. & Rivera, L., 2016b. Rupture characteristics of major and great ($M_w \geq 7.0$) megathrust earthquakes from 1990 to 2015: 1. Source parameter scaling relationships, *J. geophys. Res.,* **121,** 826–844.

Ye, L., Lay, T., Kanamori, H., Zhan, Z. & Duputel, Z., 2016c. Diverse rupture processes in the 2015 Peru deep earthquake doublet, *Sci. Adv.,* **2,** e1600581, doi:10.1126/sciadv.1600581.

Ye, L., Lay, T., Zhan, Z., Kanamori, H. & Hao, J.-L., 2016d. The isolated ~680 km deep 30 May 2015 M_w 7.9 Ogasawara (Bonin) Islands earthquake, *Earth planet. Sci. Lett.,* **433,** 169–179.

Ye, L., Kanamori, H. & Lay, T., 2018. Global variations of large megathrust earthquake rupture characteristics, *Sci. Adv.,* **4,** eaao4915, doi:10.1126/sciadv.aao4915.

Ye, L., Lay, T., Bai, Y., Cheung, K.F. & Kanamori, H., 2017. The 2017 M_w 8.2 Chiapas, Mexico, earthquake: energetic slab detachment, *Geophys. Res. Lett.,* **44**(11), 824–811, doi:10.1002/2017GL076085.

Ye, L., Lay, T., Kanamori, H. & Koper, K.D., 2013. Energy release of the 2013 M_w 8.3 sea of Okhotsk earthquake and deep slab stress heterogeneity, *Science,* **341,** 1380–1384.

Yoshimoto, M. *et al.*, 2017. Depth-dependent rupture mode along the Ecuador-Colombia subduction zone, *Geophys. Res. Lett.,* **44,** 2203–2210.

Zhan, Z., 2017. Gutenberg–Richter law for deep earthquakes revisited: a dual-mechanism hypothesis, *Earth planet. Sci. Lett.,* **461,** 1–7.

Zhan, Z., Kanamori, H., Tsai, V.C., Helmberger, D.V. & Wei, S., 2014. Rupture complexity of the 1994 Bolivia and 2013 Sea of Okhotsk deep earthquakes, *Earth planet. Sci. Lett.,* **385,** 89–96.

Zhan, Z., Shearer, P.M. & Kanamori, H., 2015. Supershear rupture in the 24 May 2013 M_w 6.7 Okhotsk deep earthquake: additional evidence from regional seismic stations, *Geophys. Res. Lett.,* **42,** 7941–7948.

APPENDIX A: CONTINUOUS PERIOD MEASUREMENT OF SEISMOGRAMS

We can show (e.g. Nakamura 1988; Kanamori 2005) that an instantaneous period $\tau(t)$ at time t of a time-series $x(t)$ over a time interval from t-(1/2)t_d to t + (1/2)t_d can be given by

$$\tau(t) = 2\pi \sqrt{\frac{\int_{t-(1/2)t_d}^{t+(1/2)t_d} x^2(t)\mathrm{d}t}{\int_{t-(1/2)t_d}^{t+(1/2)t_d} \dot{x}^2(t)\mathrm{d}t}}.$$

Fig. A1 shows two examples, one for the seismogram of the 2005 Nias, Sumatra, earthquake recorded at station PMG, and the other, the seismogram of the 2011 Tohoku earthquake recorded at station KURK. In Fig. A1, $\tau(t)$ is shown for 3 t_ds, 5, 10 and 20 s. The peak-amplitude phase and its period are marked by a vertical red line. The choice of t_d is not critical, but it should be longer than the representative period of the time-series studied. With a short t_d,

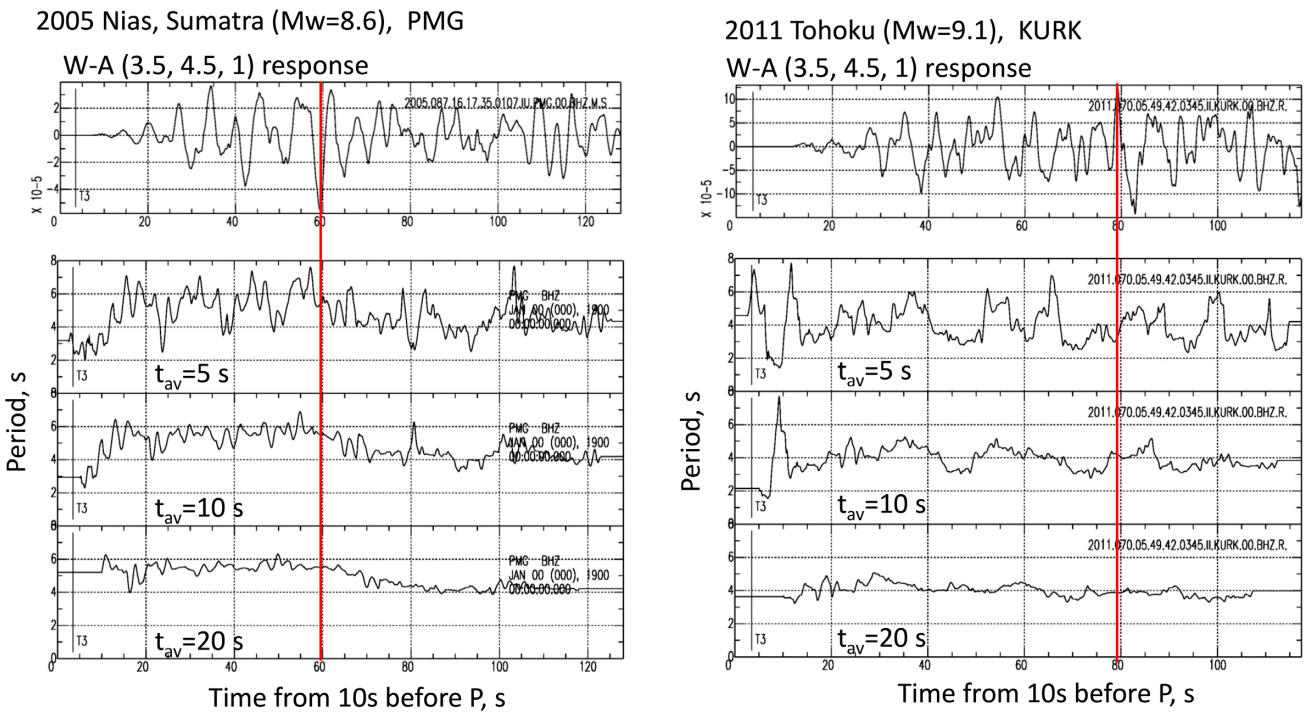

Figure A1. Two examples of continuous period determination, one for the seismogram of the 2005 Nias, Sumatra, earthquake recorded at station PMG, and the other, the seismogram of the 2011 Tohoku earthquake recorded at station KURK. The instantaneous period, $\tau(t)$, is shown for 3 t_ds, 5, 10 and 20 s. The peak-amplitude phase and its period are marked by a vertical red line.

the period varies rapidly, but regardless of t_d, we obtain a period of about 5.5 s for PMG record, and 4 s for the KURK record. In our study, we use $t_d = 5$ s, because for smaller events, the total duration of the *P*-wave window is about 10 s, and $t_d = 5$ s is appropriate. If we use the conventional methods, the zero-crossing times vary around the peak phase, and some subjective judgements would have to be made. Especially in case of the KURK record for the 2011 Tohoku earthquake, there are small wiggles around the main phase (Fig. A1), which makes the determination of the 'period' difficult. We believe that the method we use can provide an estimate of the 'period' objectively and robustly, and the 'period' thus obtained is generally consistent with that reported by seismographic observatories.

APPENDIX B: DIFFERENCE BETWEEN E_R ESTIMATED WITH A MODERN PRACTICE AND E_{R_B} ESTIMATED FROM m_B

Modern techniques for estimating radiated energy E_R generally involve integrating the energy over a broad frequency band, typically from 0 to 1 Hz. In contrast, E_{R_B} is estimated from the amplitude of a *P* wave over a period 2–5 s, essentially a single period. It is natural to question how one can possibly estimate E_R from a signal at a single period. For a general broad-band time signal, it is obviously impossible. However, we can show that because of special properties of the seismic source spectrum, E_{R_B} can be a reasonable approximation of E_R under many circumstances.

It is generally agreed that the seismic source spectrum can be represented by an ω^2 model (Aki 1967; Brune 1970)

$$\hat{M}_0(f) = M_0 f_c^2 / \left(f^2 + f_c^2\right), \tag{B1}$$

where M_0 is the seismic moment and f_c is the corner frequency. In a self-similar ω^2 model, M_0 can be written as

$$M_0 \propto \Delta\sigma f_c^{-3}, \tag{B2}$$

where $\Delta\sigma$ is a constant scaling parameter in the unit of stress. Actual data show considerable departure from the ω^2 model. For example, the slope at high frequency occasionally deviates from 2, and $\Delta\sigma$ is not constant and can vary with M_0 and other event characteristics. Thus, in general M_0 and f_c should be regarded as independent parameters.

We first proceed with the assumption that the constant $\Delta\sigma$ ω^2 model is a good representation of the average behaviour and the individual events display considerable variations around it (e.g. a factor of 5 in amplitude at a given frequency). For the ω^2 model the radiated energy can be given by (e.g. Madariaga 2009)

$$E_R \propto M_0^2 f_c^3. \tag{B3}$$

For the constant $\Delta\sigma$ model

$$M_0 \propto f_c^{-3} \tag{B4}$$

and the ω^2 model becomes a single parameter model; if a specific value is given to $\Delta\sigma$, M_0 or any single spectral ordinate can determine the entire spectrum. In our case, m_B is computed from the logarithm of the amplitude of the seismogram at a frequency f_r (typically 0.2–0.5 Hz). With the assumption that the seismogram amplitude at f_r is approximately proportional to the spectral amplitude of the moment-rate function at f_r, $\hat{a}(f_r)$, we can write

$$10^{m_B} \propto \hat{a}(f_r) \propto M_0 f_c^2, \tag{B5}$$

where f_r is assumed to be much larger than f_c for $M_w \geq 6.5$. Hereafter, we always use this assumption for simplicity. (For events with $M_w < 6.5$, small corrections are required, but for the sake of discussion here, they are not important.) Combining this with (B3) and

(B4), we have

$$E_{\rm R} \propto 10^{3m_{\rm B}} \ . \tag{B6}$$

The coefficient 3 before $m_{\rm B}$ is slightly larger than that of Gutenberg-Richter's relation, 2.4. However, this difference can be eliminated easily with minor modification of the scaling relation. For example, we can instead allow minor dependence of the stress parameter $\Delta\sigma$ on M_0,

$$\Delta\sigma \propto \left(\frac{M_0}{M_{0,\rm r}}\right)^k \Delta\sigma_{\rm r}, \tag{B7}$$

where the subscript 'r' is for a reference event and k is a constant (no longer self-similar). Then, we can derive using (B2)

$$\left(\frac{f_{\rm c}}{f_{\rm c,r}}\right) = \left(\frac{M_0}{M_{0,\rm r}}\right)^{\frac{k-1}{3}} \tag{B8}$$

with which

$$10^{m_{\rm B}-m_{B,\rm r}} = \left(\frac{\hat{a}}{\hat{a}_{\rm r}}\right) = \left(\frac{M_0}{M_{0,\rm r}}\right)\left(\frac{f_{\rm c}}{f_{\rm c,r}}\right)^2 = \left(\frac{M_0}{M_{0,\rm r}}\right)^{\frac{1+2k}{3}} = \left(\frac{E_R}{E_{R,\rm r}}\right)^{\frac{1+2k}{3(k+1)}}. \tag{B9}$$

Thus, if $k = 0.33$, then $E_R \propto 10^{2.4m_B}$ which is consistent with the Gutenberg–Richter $E_{\rm R}$ versus $m_{\rm B}$ relation. Of course, Gutenberg & Richter (1956) derived 2.4 completely empirically without using any explicit scaling relations.

The above derivation is simply meant to show that the Gutenberg–Richter relation is generally consistent with modern scaling relations, and for that reason, the energy $E_{\rm R\_B}$ estimated from $m_{\rm B}$ can be a good proxy for the radiated energy $E_{\rm R}$ if the moment-rate function has an ω^2-model-like structure. However, the source spectrum of real earthquakes can be very complex so that $E_{\rm R\_B}$ estimated from a single frequency can be significantly different from $E_{\rm R}$ if the moment-rate function has a very peculiar form. Needless to say, for any detailed study, $E_{\rm R}$ should be computed using modern practice and modern high-quality data, and $E_{\rm R\_B}$ is most useful for comparing recent events with historical events, or for reconnaissance study of recent events. We also note that if a significant difference between $E_{\rm R}$ and $E_{\rm R\_B}$ is found, it may be indicating some important special characteristics of the source spectrum, for example, a peaked spectrum.